

Radial Orbit Instability

Analysis of geometry in unperturbed and perturbed systems



Bachelor thesis at the Faculty of Physics
Ludwig-Maximilians-University Munich

Submitted by
Ludwig Maximilian Böss

Supervised by
Prof. Dr. Andreas Burkert
Dr. Rhea-Silvia Remus

Munich, 15th of September 2017

Radial Orbit Instability

Analyse der Geometrie von ungestörten und gestörten
Systemen



Bachelorarbeit an der Fakultät für Physik der
Ludwig-Maximilians-Universität München

Eingereicht von
Ludwig Maximilian Böss

Betreut von
Prof. Dr. Andreas Burkert
Dr. Rhea-Silvia Remus

München, den 15.9.2017

Contents

1. Introduction	1
1.1. Motivation	1
1.2. Radial Orbit Instability	2
1.3. Density Profiles	4
2. Method	7
2.1. Code	7
2.2. Units	9
2.3. Setup of Initial Conditions	10
2.3.1. Unperturbed Radial Orbit Instability	12
2.3.2. Rotation	13
2.3.3. Central mass	14
2.4. Numerics	15
2.4.1. Code stability	15
2.4.2. Energy conservation	17
2.5. Collisionless calculation	18
2.6. Ellipticity	20
3. Unperturbed Radial Orbit Instability	23
3.1. Dynamical Evolution	23
3.1.1. Plummer Setup	23
3.1.2. Hernquist Setup	29
3.2. Ellipticity	29
3.2.1. Plummer-Profile	30
3.2.2. Hernquist-Profile	32
3.3. Impact of resolution	33
3.3.1. Plummer profile	33
3.3.2. Hernquist profile	36
4. Perturbed Radial Orbit Instability	39
4.1. Rotation	39
4.1.1. Plummer Setup	39
4.1.2. Hernquist Setup	42
4.2. Central Mass	45
4.2.1. Plummer Setup	45
4.2.2. Hernquist Setup	47

5. Summary and Conclusion	51
I. Bibliography	55
II. List of Figures	59
III.Appendix	61
III.1. Additional Plots	61
III.1.1. Dynamical Evolution of the Hernquist Profile	61
III.1.2. Effect of central mass on the Hernquist profile	65
III.2. List of Simulations	66
III.2.1. Undisturbed ROI	66
III.2.2. Disturbed ROI	68
IV.Acknowledgements	73
V. Selbstständigkeitserklärung	75

1. Introduction

1.1. Motivation

The stability of stellar systems has always been a key question in theoretical astrophysics. Since gravitational systems with more than two bodies have no analytical solution, solving questions imposed by N-body systems relies on numerical or statistical approaches. One of these statistical approaches was first introduced by Antonov (1961) and led to the theory of Radial Orbit Instability (ROI). This section is intended to give a short motivation for an examination of ROI, a more detailed explanation of the theory will be given in the next section. For a historical overview of most papers on ROI until 2010 see Maréchal and Perez (2011).

The theory of ROI allows for an instability in systems with predominantly highly excentric radial orbits, which causes initially spherically symmetric systems to flatten and become prolate or triaxial. This led to a series of simulations to test the impact of this instability on isothermal spheres and spherically symmetric stellar systems to explain the geometric properties of elliptical galaxies (see e.g. Henon (1973); van Albada (1982); Palmer and Papaloizou (1987); Burkert (1990); Theis and Spurzem (1998)).

One of the key assumptions for ROI is that the system is collisionless, which makes the theory also applicable to dark matter halos (DMHs). This sparked a recent interest in the impact of ROI on the properties of DMHs. The result of which were that ROI might be the reason for some of the properties of the NFW density profile (Navarro et al. (1996), see Sec. 1.3), as proposed by MacMillan et al. (2006). Bellovary et al. (2008) obtained the geometric counterpart to these implications by observing the geometric properties of DMHs that had undergone ROI. While MacMillan et al. (2006) and Bellovary et al. (2008) used isolated DMHs, Ceverino et al. (2015) obtained their results with baryonic matter inside of the halo. They used their simulations to examine the influence of prolate DMHs on the shapes of their inhabiting galaxies.

The purpose of this thesis is to show a connection between the ellipticity of the resulting stellar system and the initial energy relation. This connection will be established in the unperturbed systems and then compared to systems with induced perturbations. These perturbations will be an added rotational velocity v_ϕ and a compact central mass with different masses M_\bullet .

1.2. Radial Orbit Instability

The purpose of this section is to give a short introduction to the basic concept of Radial Orbit Instability. Since this thesis is not about an analytical approach to ROI, but rather a phenomenological analysis of its impact on different spherical stellar systems, the mathematical concepts will be kept brief. For in depth analysis of the mathematical properties see the cited papers.

The most intuitive approach to the cause of Radial Orbit Instability is given by Palmer and Papaloizou (1987), who base their explanation on the work by Lynden-Bell (1967). This is best summed up by Maréchal and Perez (2011): "An axisymmetric perturbation of the potential [...] could influence a star's orbit and lengthen it, which tends to align orbits along the perturbation.". One explanation for this axisymmetric perturbation is given by Burkert (1990), who states that elliptical galaxies undergo a short initial star-burst phase, after which the system experiences a violent collapse phase. Small initial inhomogenities cause the axisymmetric perturbations, as stars come closer to each other, which causes the orbits of some stars that follow one of these inhomogenities to align. This concept is later emphasised by Polyachenko (1992b), with the constraint of orbit orientation. He states that the torque that alters the orbital angular momentum, induced by the forced alignment along the perturbation, has different effects on the system, dependent on its direction. If this torque forces the orbital precession rates of the stars to change in the same direction, it leads to a bar-like structure, while a opposite force causes the instability to oscillate.

The "tuning-fork" diagram taken from his original paper can be seen in Fig. 1.1. The top-right image displays the resulting instability if the orbit precession rates are pushed in the same direction, the bottom-right image displays the resulting oscillation if they are not. This prolate, bar-like shape is the prominent feature of Radial Orbit Instability that

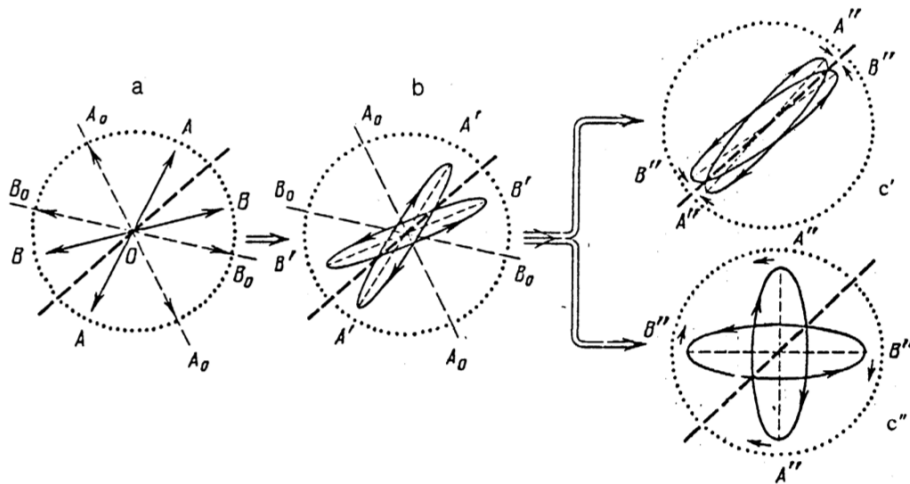


Figure 1.1.: "Tuning-Fork" Diagram: Display of the two different possible developments of the instability, as presented by Polyachenko (1992b)

can be observed in position-space.

Bellovary et al. (2008) give special importance to these torques in the further development of ROI. They state that, as the system collapses and stars feel the torque from neighbouring stars the loose angular momentum. This brings the stars on a smaller orbit and causes the density in the inner region of the system to increase.

Since this interaction solely depends on gravity, it is also applicable to dark matter halos. The work by MacMillan et al. (2006), which will be of importance later, uses this concept to explain the slope of the NFW-profile (see Section 1.3 for the description of the profile).

Analytical approaches tried to find a threshold for the onset of ROI. The first proposal of such a threshold was given by Polyachenko and Shukhman (1981), who performed a fourier analysis of the perturbations and analysed them with a matrix-method.

Using this approach they found a criterion for stability, the "russian stability criterion", ξ in this thesis

$$\xi = \frac{2T_r}{T_\perp} > 1, 7 \pm 0, 25. \quad (1.1)$$

Here T_r and T_\perp are the kinetic energy in radial direction and perpendicular to radial direction, respectively. The value for ξ is not coherent over different studies. Merritt and Aguilar (1985) used the same method as Polyachenko and Shukhman (1981) and found a sharp transition between stability and instability at

$$\xi \approx 2.5 \quad (1.2)$$

while Trenti and Bertin (2006) soften this sharp transition to

$$\xi \approx 2.5 - 2.9. \quad (1.3)$$

An alternative approach towards a parameter for the onset of ROI is used for example by Bellovary et al. (2008). The so-called anisotropy parameter

$$\beta = 1 - \frac{\sigma_\phi^2}{2\sigma_r^2} \quad (1.4)$$

depends on the relation between σ_ϕ and σ_r , hence the velocity dispersion in ϕ - and r -direction respectively.

For more work on analytical solutions to ROI see: Palmer and Papaloizou (1987), Polyachenko (1991), Polyachenko (1992a), Polyachenko et al. (2011), Polyachenko and Shukhman (2015), Polyachenko and Shukhman (2016) and Polyachenko and Shukhman (2017).

This thesis will work with a parameter for the onset of ROI as a function of the initial virial parameter $\eta_{vir,0}$, derivation of which will be subject of Sec. 2.3.1.

1.3. Density Profiles

The goal of this thesis is to analyse the impact of ROI on the shape of spherical stellar systems, characterised by two different density profiles. The properties of these density profiles will be discussed in this section.

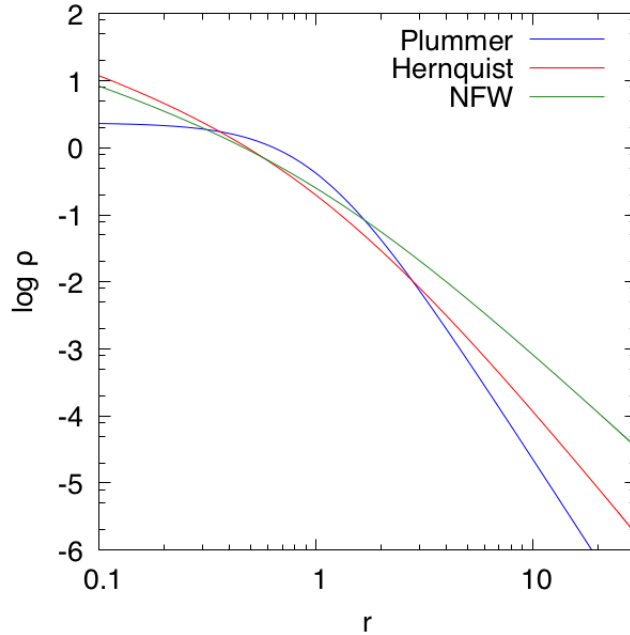


Figure 1.2.: Ideal plots of the density profiles

The first density profile in question was discovered by Plummer (1911) and will be henceforth referred to simply as Plummer profile. Plummer derived this density profile by counting stars in high-resolution images of globular clusters, which required exceptional accuracy for the time. From this method he obtained the density distribution

$$\rho_P(r) = \frac{3M}{4\pi a^3} \cdot \left(1 + \frac{r^2}{a^2}\right)^{-\frac{5}{2}} \quad (1.5)$$

where M is the total mass and a is a scaling length and in this case a measure of the half-mass radius (HMR)

$$r(M_{1/2}) = 1.3 \cdot a \quad (1.6)$$

also referred to as core-radius. The half-mass radius marks the radius within which half of the total mass is contained. A plot of the density profile can be seen in Fig. 1.2. Here the values for M and a are chosen to be $M = 1$ and $a = 1$.

The most prominent feature of the profile is an inner region of constant and finite density. After $r = 1$ the density drops constantly, with a slope of $\rho \sim r^{-5}$. This ensures that the total mass enclosed by the profile is finite.

The second density profile that will be tested for the impact of ROI is the density profile proposed by Hernquist (1990). Hernquist introduced this density profile to present a potential-density pair that closely approximates the de Vaucouleurs $R^{1/4}$ -law for elliptical galaxies. While the $R^{1/4}$ -law describes the surface-brightness and hence the stellar mass of elliptical galaxies very nicely, it has the disadvantage of being of purely observational nature. This leads to the problem that essential values, like the escape velocity or the free-fall time, can't be directly derived from the profile. For that reason Hernquist calculated an analytical solution for a close approximation to the de Vaucouleurs law that follows the equation

$$\rho_H(r) = \frac{M}{2\pi} \cdot \frac{a}{r(r+a)^3}. \quad (1.7)$$

The inner region of the profile grows in density, in contrast to the Plummer profile. This causes the density to diverge, as $r \rightarrow 0$, which of course is not possible in real stellar systems. Compared with the Plummer profile the density decreases faster until $r \approx 12$. After that the Hernquist profile decreases slower, which causes the outer regions of the profile to be more dense.

The last density profile discussed in this thesis is the NFW profile, as proposed by Navarro et al. (1996). Even though there were no simulations conducted with this profile, recent studies like those of MacMillan et al. (2006) have tried to explain the properties of the NFW profile as a result of ROI. Therefore it plays an important role in the field of ROI research.

This profile was found by Navarro et al. (1996), who fitted the dark matter halos observed in numerical cosmological simulations with an approximated density curve. It is therefore the only density profile of the three to not be found as a result of observations in stellar systems, which of course is due to the fact that dark matter can't be observed directly. The profile follows the equation

$$\rho_{NFW}(r) = \frac{\rho_a}{r(r+a)^2}. \quad (1.8)$$

This profile behaves as $\rho \sim r^{-1}$ in the core, $\rho \sim r^{-2}$ at $r = a$ and like $\rho \sim r^{-3}$ in the outskirts of the system and is therefore more closely related to the Hernquist profile than the Plummer profile.

The knowledge of the properties of the density profiles can be used for various calculations. One of these calculations is the obtaining of a free-fall time $t_{ff}(r)$, which will be discussed in more detail in Sec. 2.5. As the free-fall time at a given radius is dependent on the mass inclosed within that radius, it depends on the properties of the density profiles.

2. Method

2.1. Code

The underlying code of this work is a N-body code by Lars Hernquist, written in the FORTRAN '77 language. It was originally published in 1987 (Hernquist, 1987) and revised in 1996. The code is based on the treecode concept introduced by Barnes and Hut (1986) and uses a self-starting Leapfrog integrator. Both of these concepts will be discussed in this section.

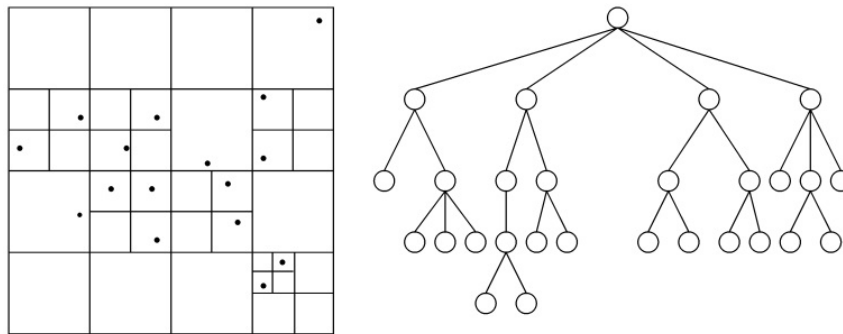


Figure 2.1.: Concept of a Treecode. Image Credit: Nyland et al (1993)

The general concept of a treecode as introduced by Barnes and Hut (1986) is displayed in Fig. 2.1. At each timestep of the simulation a grid of 3-dimensional cubic cells is overlaid over the system. If one cell of the initial grid contains more than one particle, that cell is subdivided by cutting its edge length in half, which cuts the original cell into eight cubic subcells. This process is repeated until each cell contains only one particle. By discarding the empty cells, this leads to the hierarchical tree-like structure displayed on the right side of Fig. 2.1. While setting up this grid takes time, following Barnes and Hut (1986) the required time is of the order $\mathcal{O}(N \log N)$, the advantage is the possibility to combine distant cells into one. That way the force on an individual particle p can be calculated as the force of the center of mass of a cell on that particle. To get a function for the combining or subdividing of cells, a parameter θ is defined that corresponds to an opening angle. This concept is most evident if viewed from the perspective of a bigger cell with more than one particle. If $\theta > l/D$, with l being the length of the cell and D being the distance of the center of mass of the cell to the particle whose force is being calculated, the cell is kept as it is. The resulting force on the particle is then that of a pseudo-particle with the combined mass of all particles in the cell, at the center of mass of that cell. If $\theta < l/D$ the cell is subdivided into eight subcells and the process is repeated. That way

closer cells are smaller and contain less particles, while more distant cells are larger and contain more particles. The combining of cells obviously leads to an error, as the force is computed for the center of mass and not for the real positions of the particles, but this error can be controlled by changing θ to smaller values, if necessary. Following Hernquist (1987) this error is less than 1% in comparison to a direct sum over the particles.

This loss in accuracy is compensated by a significant cutdown in computing time, as Fig. 2.2 shows. While calculating the individual forces between the particles would require $\frac{1}{2}N(N-1)$ calculations, so $\mathcal{O}(N^2)$, the tree method reduces that to $\mathcal{O}(N \log(N))$. For particle numbers of $N \approx 10^5$, as used in this thesis, that leads to a reduction of computing time by 4 orders of magnitude.

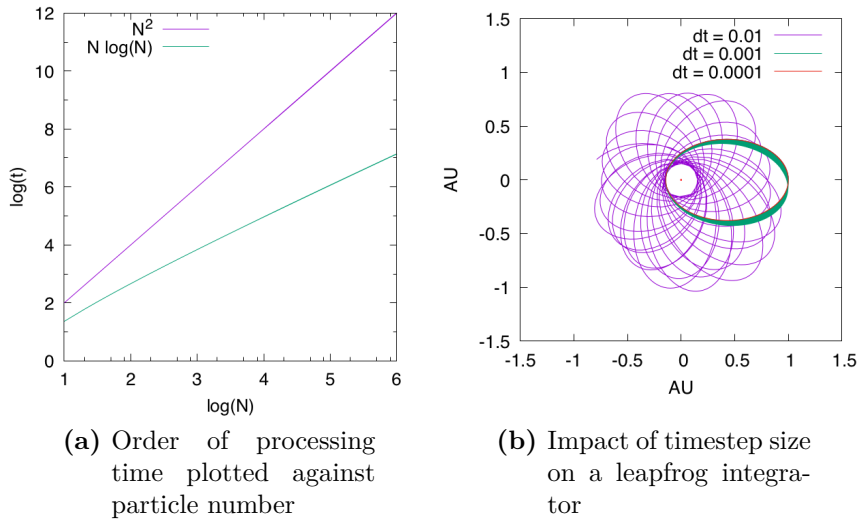


Figure 2.2.: Code Properties: Order of processing time (left) and impact of timestep size on a leapfrog integrator (right)

A Leapfrog integrator is a numerical improvement to the classic euler integrator. The classic euler integrator calculates the acceleration on a particle and then multiplies the resulting vector of acceleration with the timestep size to obtain a velocity vector. Once the velocity is obtained the next position for the particle can be obtained by multiplying the velocity with the same timestep size.

$$t_{n+1} = t_n + \Delta t \quad (2.1a)$$

$$\vec{v}_{n+1} = \vec{v}_n + \vec{a}_n \cdot \Delta t \quad (2.1b)$$

$$\vec{x}_{n+1} = \vec{x}_n + \vec{v}_{n+1} \cdot \Delta t \quad (2.1c)$$

This causes a problem if the chosen timestep size is too big. For positions with high acceleration, the particle is still multiplied by the same fixed timestep, which causes the particle to overstep his actual next position. Once this overstepping has happened, all consecutive accelerations will be smaller than they should be, which in turn causes the particle to spiral outwards. This also leads to poor energy conservation.

To account for this problem, a Leapfrog integrator is used. In contrast to the euler integrator, a Leapfrog integrator takes an initial half timestep and calculates the acceleration- and velocity vector at this point.

$$t_{n+1} = t_n + \Delta t \quad (2.2a)$$

$$\vec{v}_{n+1} = \vec{v}_n + \vec{a}_{n+1/2} \cdot \Delta t \quad (2.2b)$$

$$\vec{x}_{n+1/2} = \vec{x}_{n-1/2} + \vec{v}_n \cdot \Delta t \quad (2.2c)$$

This results in a tangential velocity vector at the $\frac{\Delta t}{2}$ -point. Once the velocity vector is obtained, it is multiplied by Δt to get the position vector. This position vector is then evaluated on the initial starting point. For a circular orbit this causes the position vector to always end up on the ideal circle. In elliptical orbits, the timestep size gains importance. If the timestep size is sufficiently small, the process works the same way as in the circular orbit. For bigger timesteps the ellipses start to precess, as shown in Fig. 2.2 b). For sufficiently small timesteps, both energy loss and orbit precession is minimised. The plot for the Leapfrog integrator was obtained from another code with a central point mass and only serves as an example. The matter of energy conservation of this code will be discussed in Sec. 2.4.2.

2.2. Units

The Code is in itself scale-free, so physical units can be chosen freely to some degree. The code imposes that $G = 1$, so all units have to be calculated from that restriction. All setups (except for those with a compact central mass) also use $M_{tot} = 1$.

Units for a globular cluster with a Plummer density profile are chosen to be as length- and mass unit respectively: $l_{unit} = 10pc$ and $m_{unit} = 10^6 M_\odot$. Deriving the assorted time-unit from these restrictions is easiest by directly calculating the rotational velocity and then calculating the time-unit from that velocity.

$$v^2 = \frac{G \cdot M}{R} \quad (2.3)$$

Since all of the units in that fraction are equal to 1 the velocity in code-units is

$$v = \sqrt{\frac{G \cdot m_{unit}}{l_{unit}}} = 1 v_{unit} \quad (2.4)$$

and

$$v_{unit} = \frac{l_{unit}}{t_{unit}}. \quad (2.5)$$

This equation solved for t_{unit} yields:

$$t_{unit} = \left(\frac{l_{unit}^3}{G_{cgs} \cdot m_{unit}} \right)^{\frac{1}{2}} \quad (2.6)$$

Inserting the chosen length- and mass units into equation 2.6 returns the numerical value

$$t_{unit} = 1.4877 \cdot 10^{13} s \approx 4.7143 \cdot 10^5 yr \approx 0.5 \cdot 10^6 yr \quad (2.7)$$

This leads to a velocity unit:

$$v_{unit} = \frac{l_{unit}}{t_{unit}} \approx 6.5726 \cdot 10^{-2} \frac{pc}{yr} \quad (2.8)$$

For a elliptical galaxy which follows a Hernquist density distribution the initial units look rather different. Large elliptical galaxies usually have a total mass of $M_{tot} \approx 10^{12} M_{\odot}$ and reasonable length-scales are in the kpc regime. Since the proportions of these changes cancel out in equation 2.6 the numerical values for both systems are the same.

Sec. 4.1 will require a rotation Ω that follows the equation

$$\Omega = \frac{q \cdot \sigma(R)}{R} = \frac{q \cdot v_{unit}}{l_{unit}} \quad (2.9)$$

which corresponds to a unit for Ω of

$$\Omega_{unit} = q \cdot 6.5726 \cdot 10^{-3} \frac{1}{yr}. \quad (2.10)$$

To keep the plots clean all results of this thesis will be discussed in code-units unless otherwise indicated by the explicit use of physical units.

2.3. Setup of Initial Conditions

As previously mentioned in section 2.1 the initial conditions were set up with an additional code that generates a system in equilibrium where all particles follow a given density-distribution. This section will follow the process of setting up the initial conditions for a Plummer sphere. The process for the Hernquist sphere is the same, except for a different energy density function $f(E)$.

To obtain such a system one first needs to define a maximum system-radius R_{sys} and an asymptotic mass M_{sys} as the total mass which is enclosed in the system as $r \rightarrow \text{inf}$. In all simulations the system radius was chosen to be $R_{sys} = 50$ and all but the central mass simulations use $M_{sys} = 1$. The particle masses for all simulatons with equal masses are

then easily obtained by dividing $M(R_{sys})$ by the number of particles N_p . $M(r)$ in the Plummer and Hernquist models follow

$$M_P(r) = \frac{M_{sys}}{(r^2 + a^2)^{3/2}} \cdot r^3 \quad (2.11)$$

$$M_H(r) = \frac{M_{sys}}{(r + a)^2} \cdot r^2 \quad (2.12)$$

respectively, where a is a constant, in this case $a = 1$. With $N_p = 80.000$ this leads to $m_P = 1.24925 \cdot 10^{-5}$ and $m_H = 1.20146 \cdot 10^{-5}$ in code units. After the initial boundaries are set, the radial component of the particle-position is generated by multiplying a random number ι with R_{sys} .

Next the escape velocity from the core radius

$$v_{esc}(a) = \frac{2GM}{a} \quad (2.13)$$

is calculated and again multiplied by a random number. To check whether the generated particle is bound to the system the total energy per unit mass is calculated. If the energy is negative the code proceeds, if not, the previous two steps are repeated. The next step is to check if the generated particle follows the energy density equation of the different profiles and therefore follows the density profiles.

For the Plummer model the energy density equation is

$$f(E) = \left(\frac{r}{a}\right)^2 \cdot \left(\frac{v}{v_{esc}(a)}\right) \cdot \frac{(-E)^{7/2}}{const} \quad (2.14)$$

where the constant is chosen in such a way that $f(E) \leq 1$. These calculations have only set up the particle in one dimension, the other two dimensions need to be added. Since the system is by definition spherically symmetric it is most reasonable to choose spherical coordinates to do so. For that θ and ϕ components need to be added. While ϕ is directly generated by multiplying 2π by a random number, θ is a little more complicated. Instead of calculating $\theta \in \{0, \pi\}$ it is easier to directly calculate $\cos(\theta) \in \{-1, 1\}$. A random distribution for $\cos(\theta)$ is obtained by using the equation

$$\cos(\theta) = 2 \cdot \iota - 1 \quad (2.15)$$

where ι is a random number between 0 and 1. Then $\sin(\theta)$ follows from

$$\sin(\theta) = \sqrt{1 - \cos(\theta)^2} \quad (2.16)$$

and the sign of $\sin(\theta)$ is added via

$$\sin(\theta) = \frac{\iota}{|\iota|} \cdot \sin(\theta) \quad (2.17)$$

Once this is completed in position-space, the same procedure is repeated to get a random distribution in the velocity-space. After all free parameters are filled the system is transferred back into cartesian coordinates by using

$$x = r \cdot \sin(\theta) \cdot \cos(\phi) \quad (2.18a)$$

$$y = r \cdot \sin(\theta) \cdot \sin(\phi) \quad (2.18b)$$

$$z = r \cdot \cos(\theta) \quad (2.18c)$$

for position and velocity coordinates respectively. Once the cartesian coordinates are known the computing can be initiated.

There is however a small problem with the randomness of the beforementioned numbers. Since the random number generator is seeded, it will always produce the same sequence of pseudo-random numbers and hence always distribute the particles in the same way. This usually undesirable effect holds a great advantage in this case: The system that is tested for stability is always the same one, which means that the different tests are less vulnerable to numerical effects caused by the random number generator. Hence the inhomogenities of the initial density profiles are always the same and the evolution of the systems are perfectly comparable to each other.

2.3.1. Unperturbed Radial Orbit Instability

To get a setup for the observation of unperturbed ROI an approach similar to Trenti and Bertin (2006) was chosen. The initial velocities were rescaled by multiplying the equilibrium configuration by a constant factor $\chi < 1$ so that

$$v(t = 0) = \chi \cdot v_{eq}. \quad (2.19)$$

This leads to an initial collapse and causes ROI to develop, if the initial conditions allow for an alignment of orbits, as described in Section 1.2.

To get a quantifying measure for the energy properties of these initial conditions, the parameter $\eta_{vir,0}$ is introduced. Since the systems are set up to be in equilibrium they follow the virial equation

$$2E_{kin} = |E_{pot}| \quad (2.20)$$

with E_{kin} being the kinetic energy and E_{pot} being the potential energy of the system. From this equation the virial coefficient η_{vir} is obtained

$$\eta_{vir} \equiv \frac{2E_{kin}}{|E_{pot}|}. \quad (2.21)$$

For a system in equilibrium this means that $\eta_{vir,eq} = 1$. To get a more intuitive scaling factor for the simulations than χ , $\eta_{vir,0}$ is introduced by inserting χ into equation 2.21

$$\eta_{vir,0} = \frac{m \cdot (\chi \cdot v_0)^2}{|E_{pot}|} = \chi^2 \cdot \eta_{vir,eq} = \chi^2. \quad (2.22)$$

Since for the rest of this thesis will work mostly with $\eta_{vir,0}$, the shorthand η_{vir} is introduced. Unless otherwise stated this describes the fraction of $\eta_{vir,eq}$ in the initial conditions of the simulation.

As η_{vir} is a function of kinetic energy and the kinetic energy of particles can be associated with temperature, by relating to statistical physics and the movement of particles in a volume, the terms "dynamically warm" and "dynamically cold" will be used in this thesis. Hereby "dynamically warm" relates to systems with a higher virial ratio in the initial conditions, while "dynamically cold" relates to systems with smaller initial virial ratio. As the system collapses and proceeds to find a new equilibrium state, the particle's potential energy will be turned into kinetic energy and the system will warm up. This is due to energy conservation and the system will be in a new equilibrium state as $\eta_{vir}(t) \rightarrow 1$.

2.3.2. Rotation

For the rotation setup a rigid body rotation was added to the initial velocity distribution. The requirement was that the rotation satisfied the equation

$$R \cdot \Omega = q \cdot \sigma(R_{sys}) \quad (2.23)$$

where $\sigma(R_{sys})$ is the initial velocity dispersion at the outer radius of the system and q is a constant. The values of q were varied to test the impact of an initial rotation on the development of ROI. With the average $\sigma(R_{sys}) \approx 0.03$ taken from the initial conditions of the Plummer system and a benchmark of $q = 0.2$ this leads to

$$\Omega = \frac{q \cdot \sigma}{R_{sys}} \approx 0.0001. \quad (2.24)$$

To add a rotational velocity to the individual particles it is most efficient to do so while the system is still being set up in spherical coordinates. That way a v_ϕ can be added to each particle before it is transferred back into cartesian coordinates. Since the required rotation was that of a rigid body, v_ϕ must be proportional to the particle distance from the rotation axis, in this case the z-axis.

$$v_\phi = r_z \cdot \Omega \quad (2.25)$$

Here the distance from the rotation axis is r_z , where r_z is defined as

$$r_z = r \cdot \sin\theta. \quad (2.26)$$

Since the particle is still in spherical coordinates, both r and θ are already known and can be used to find v_ϕ . After v_ϕ has been found the new velocity components can be calculated from

$$v'_x = v_x - v_\phi \cdot \sin\phi \quad (2.27a)$$

$$v'_y = v_y + v_\phi \cdot \cos\phi \quad (2.27b)$$

$$v'_z = v_z \quad (2.27c)$$

The signs for v_ϕ are chosen in such a way that the resulting rotation is counter-clockwise, looking down on the system along the z-axis. A plot of the added velocities can be seen in fig. 2.3.

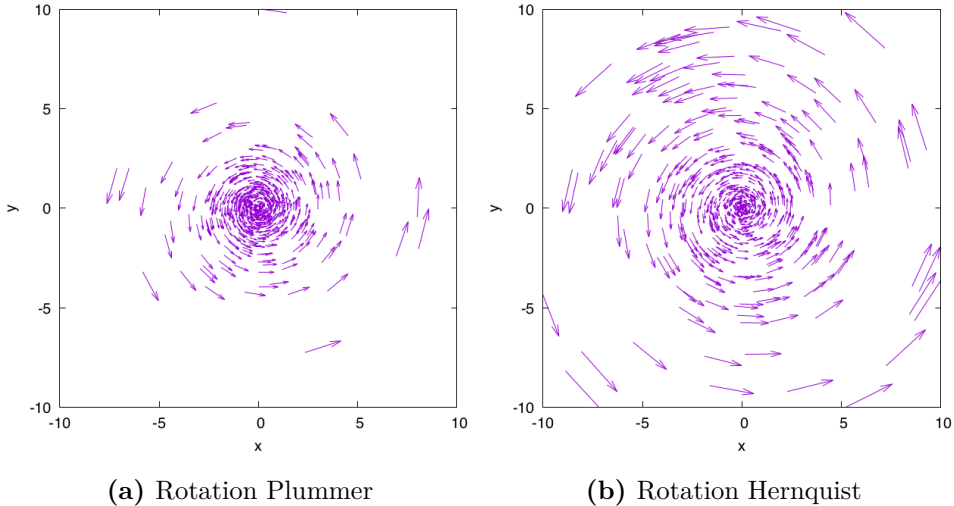


Figure 2.3.: The vectors indicate the direction and magnitude of the added rotational velocity. Plotted are only a small fraction of the particles. The signs in the transformation lead to a counter-clockwise rotation around the z-axis.

2.3.3. Central mass

As discussed by Kulkarni et al. (1993) and observed by Maccarone et al. (2007) and Chomiuk et al. (2013), there is strong evidence of black holes in globular clusters. Following Kulkarni et al. (1993)'s assumption that these black holes settle to the core of a GC due to dynamical friction on timescales $\sim 10^8 yr$, a central mass was positioned at the very center of the Plummer profile. Since there is also strong evidence for supermassive black holes (SMBHs) in the center of elliptical galaxies, as observed for example by Hlavacek-Larrondo et al. (2013)), the assumption of a compact central mass in a Hernquist profile

is also justified.

The mass of that object was varied over two orders of magnitude from $M_{\bullet} = 10^2 m$ to $M_{\bullet} = 10^4 m$, with m being the respective particle mass of the systems. To test the influence of a massive point-mass on the development of ROI, the initial velocities were again multiplied by a constant factor $\chi < 1$, as described in Section 2.3.1.

2.4. Numerics

This chapter is intended to discuss some of the numeric properties of the code, like stability of the initial conditions for an equilibrium setup and the error induced by different timestep sizes.

2.4.1. Code stability

To test the stability of the initial conditions against changes in softening length, a number of high-resolution tests with equilibrium initial conditions were conducted. The goal of these tests was to see whether any significant 2-body interaction and hence clumping or scattering in the densest regions would occur with a smaller softening length. This would lead to changes in the density profile over the time of the simulation. Clumping would increase the density in the central regions and scattering would decrease it, while increasing the density of the outer regions as time progresses. Fig. 2.4 and Fig. 2.5 show the results of the conducted test for the Plummer and Hernquist spheres respectively. ϵ indicates the softening length, so the length at which the gravitational acceleration is damped

$$\vec{a}_i = \frac{G \cdot m_j}{(|\vec{r}_i - \vec{r}_j|^2 + \epsilon^2)^{\frac{3}{2}}} \cdot \vec{r}_i \quad (2.28)$$

and has nothing to do with the ellipticities $\epsilon_{1,2}$ that will be discussed later. Softening is implemented to stop the acceleration from diverging as the particle distance $|\vec{r}_i - \vec{r}_j|$ goes to zero.

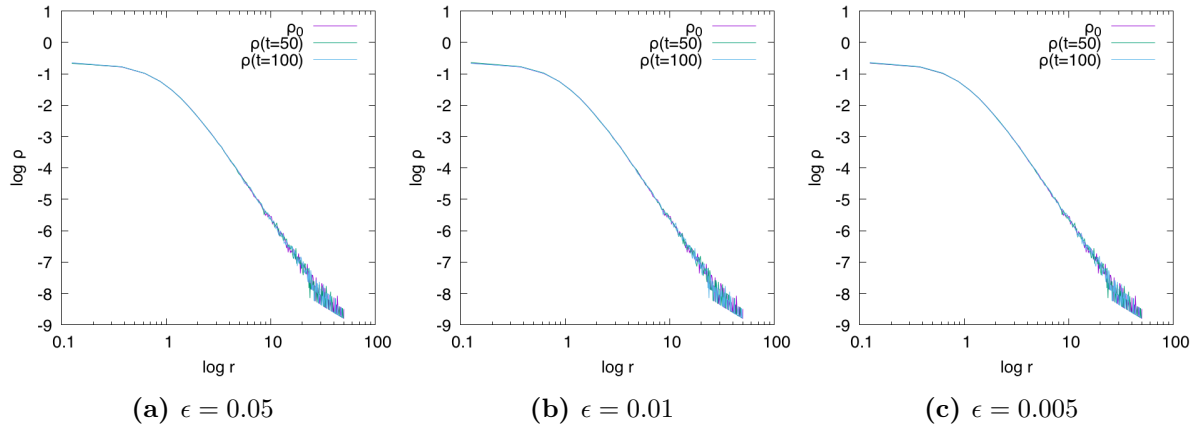


Figure 2.4.: Stability of the Plummer-Profile against change in the softening-length ϵ

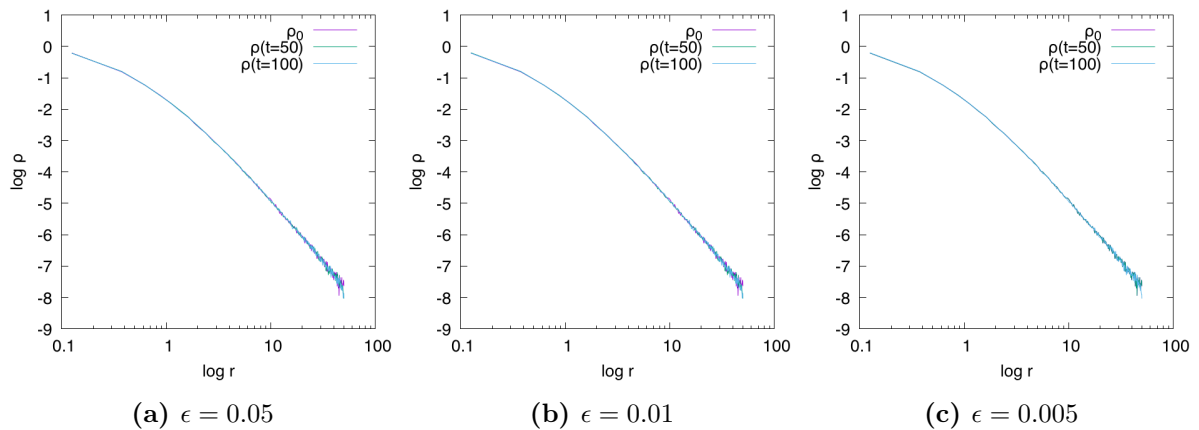


Figure 2.5.: Stability of the Hernquist-Profile against change in the softening-length ϵ

As can be seen quite clearly, the changes in the density distribution are negligible. The small fluctuations in the outer radii are due to the finite number of particles. As the density decreases with greater radius, the number of particles in the outer shells also decreases. Since the particles constantly move into and out of the shells, a changed number of particles has a great impact on the density in that radial shell. This causes the density in this shell to fluctuate purely by chance, which is a purely numerical effect without physical implications.

2.4.2. Energy conservation

This work will briefly discuss the impact of different resolution, in term of timestep size and softening length, on the resulting ellipticities of the systems. To see if the different softening lengths and timestep sizes will have a great impact on energy conservation, the simulations were evaluated in that regard. The result of a direct comparison between the high-resolution and low-resolution simulation of the Plummer sphere with $\eta_{vir} = 6.25 \cdot 10^{-2}$ can be seen in Fig. 2.6. This system will be discussed in more detail in Sec. 3.1.1.

While the high-resolution simulation stays very constant over the entire simulation with a change in total energy of

$$|\Delta E_{tot}| = 2.223 \cdot 10^{-9} \quad (2.29)$$

the lower resolution simulation drops from the initial energy to a lower level, which is nevertheless quite constant over the rest of the simulation.

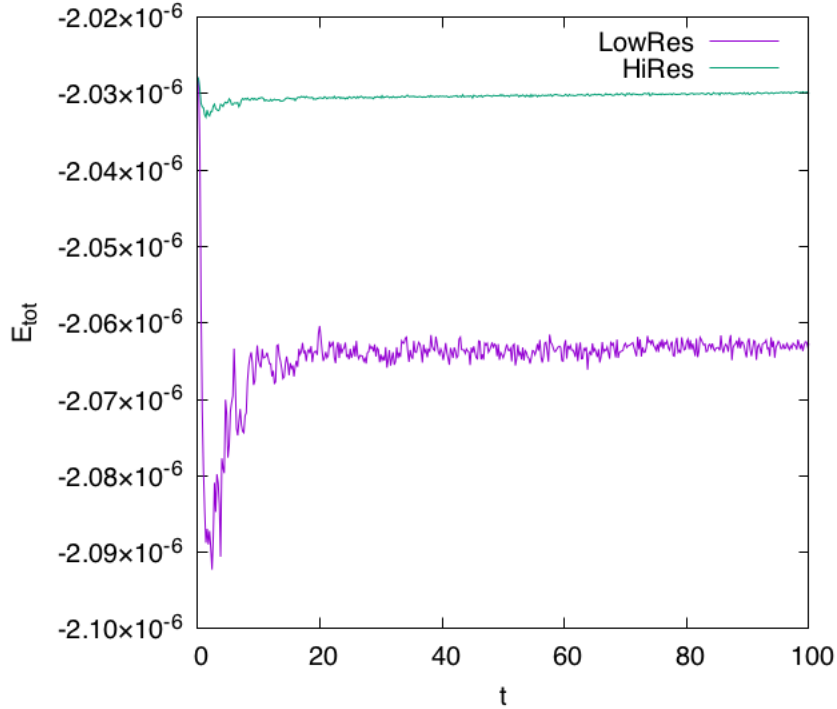


Figure 2.6.: A direct comparison between the development of the total energy in the high-resolution and low-resolution simulation "P-HighRes-0,25" and "P-0,25" (see Sec. III.2.1 for Parameters).

The low-resolution change in total energy is

$$|\Delta E_{tot}| = 3.491 \cdot 10^{-8} . \quad (2.30)$$

The loss of total energy for the high resolution simulation corresponds to $\mathcal{O}(0.1\%)$ and for the low-resolution simulation to $\mathcal{O}(1\%)$. As can be seen in Fig. 2.7 this difference in energy conservation is very small compared to the actual energies. It is therefore justified to use the results of the lower resolution simulations. Problems with differences in resolution will be discussed in Sec. 3.3.

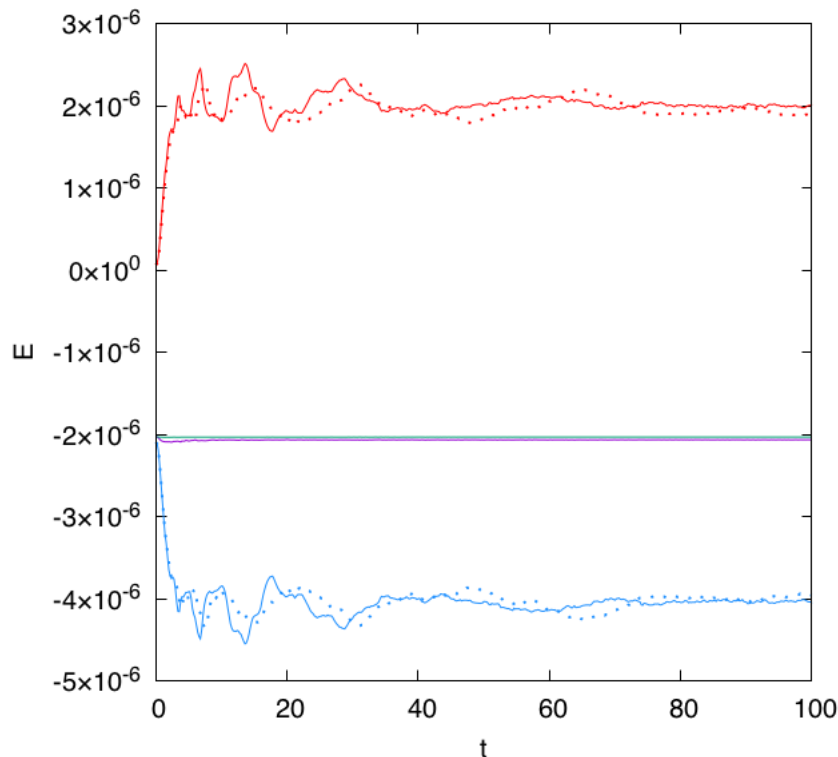


Figure 2.7.: Kinetic-, potential and total energy are plotted over the entire simulation-time. The green and purple line in the center correspond to the lines for high- and low resolution in Fig. 2.6 with the same colors. The red lines resemble kinetic energy, while the blue lines resemble potential energy. Solid and dashed lines correspond to high- and low resolution, respectively.

2.5. Collisionless calculation

As mentioned in the introduction, the ROI can only be observed in collisionless systems. To justify a collisionless calculation, the run-time of the simulation must be small compared to the relaxation time of the stellar system. The relaxation time is defined as the time on which collisions and scattering are not negligible as an effect which causes a system to become randomly distributed. Following Binney and Tremaine (2011) the

relaxation time is defined as

$$t_{relax} \simeq \frac{0.1N}{\ln(N)} \cdot t_{cross} \quad (2.31)$$

where N is the total number of particles in the system and t_{cross} describes the crossing-time, the average time it would take a particle to cross the system. The crossing time for a system in equilibrium is calculated as

$$t_{cross} = \frac{2 \cdot r}{\langle v \rangle} . \quad (2.32)$$

These equations are solved for the Plummer and Hernquist systems respectively. The initial conditions for the Plummer system yield $r \approx 50$ and $\langle v \rangle \approx 0.5$, which leads to

$$t_{cross} \approx 200 . \quad (2.33)$$

Using this result in eq. 2.31 results in a relaxation time for a Plummer system with $N = 80000$ particles

$$t_{relax} \sim \frac{0.1N}{\ln(N)} \cdot t_{cross} \approx 708.6 \cdot t_{cross} \approx 1417200 . \quad (2.34)$$

For the Hernquist system in equilibrium r and N stay the same and $\langle v \rangle$ is found to be

$$\langle v \rangle \approx 0.37 . \quad (2.35)$$

Solving the equation for relaxation time with these variables results in

$$t_{relax} \approx 191513.5 . \quad (2.36)$$

Since the dynamically coldest systems have very small initial velocities, the crossing time changes, as $\langle v \rangle$ decreases. To make sure that collisions can still be neglected, a worst-case calculation will be conducted. For this worst-case calculation one can assume that $\langle v(t=0) \rangle \approx 0$ and therefore the crossing time is $t_{cross}(r) = 2 \cdot t_{ff}(r)$, with $t_{ff}(r)$ being the free-fall time at a given radius. Additionally, since the calculations for the ellipticity will be performed within the half-mass radius $r(M_{1/2})$ (for shorthand $r_{1/2} \equiv r(M_{1/2})$ in this calculation) the relaxation time for that radius is more important than that for the entire system radius. The free-fall time is defined as

$$t_{ff}(r) = \sqrt{\frac{3\pi}{32G\rho(r)}} . \quad (2.37)$$

Solving this equation within the half-mass radius leads to

$$t_{ff} = \sqrt{\frac{3\pi}{32G\rho}} = \sqrt{\frac{3\pi V}{32GM}} = \sqrt{\frac{4\pi^2 r_{1/2}^3}{32 \frac{M}{2}}} = \sqrt{\frac{8\pi^2 r_{1/2}^3}{32}} = \frac{\pi}{2} \cdot r_{1/2}^{\frac{3}{2}} \quad (2.38)$$

where $M = 1$ and $G = 1$ was used. With $r_{1/2} \approx 1.3$ for the Plummer system this results in

$$t_{ff} \approx 2.33 \quad (2.39)$$

and hence to a relaxation-time of

$$t_{relax} \approx 3302. \quad (2.40)$$

For the Hernquist system the initial half-mass radius is $r_{1/2} = 2.26$ which leads to

$$t_{ff} \approx 5.34 \quad (2.41)$$

and a relaxation-time of

$$t_{relax} \approx 7568 \quad (2.42)$$

These solutions lead to the assumption that at a simulation time of $t_{max} = 100$ relaxation caused by collisions and scattering can be neglected. Furthermore, as $t = 100$ corresponds to $20 \cdot t_{cross}$ in the Plummer system and $10 \cdot t_{cross}$ in the Hernquist system, the runtime is therefore long enough to be able to analyse the newly found equilibrium after the initial collapse.

2.6. Ellipticity

To observe the geometric shape of the central region of the individual systems, a similar approach to Bellovary et al. (2008) was chosen. Like in the work of Bellovary et al. (2008) the inertia tensor was calculated within a fixed radius. In this case the half-mass radius, as it is a property that can be both easily calculated and observed. The next step was to obtain the eigenvalues (λ_i) of the inertia tensor

$$I_{ij} = \sum_k m_{(k)} (\delta_{ij} r_{(k)}^2 - x_{i(k)} x_{j(k)}) \quad (2.43)$$

where k is the summation index for all particles and $i(j)$ runs over the cartesian coordinates of the individual particles. While Bellovary et al. (2008) use these eigenvalues to observe the development of the axis of inertia over time, here the intrinsic ellipticities were calculated following Obreja et al. (2016). With the eigenvalues sorted as $\lambda_1 \leq \lambda_2 \leq \lambda_3$, the lengths of the three semiaxes $a \geq b \geq c$ follow the equation

$$a^2 + b^2 + c^2 = \frac{5(\lambda_1 + \lambda_2 + \lambda_3)}{2} \quad (2.44)$$

and hence

$$\frac{a^2}{b^2} = \frac{\lambda_3 + \lambda_2 - \lambda_1}{\lambda_1 + \lambda_3 - \lambda_2}, \quad (2.45a)$$

$$\frac{a^2}{c^2} = \frac{\lambda_3 + \lambda_2 - \lambda_1}{\lambda_1 + \lambda_2 - \lambda_3}, \quad (2.45b)$$

$$\frac{c^2}{b^2} = \frac{\lambda_1 + \lambda_2 - \lambda_3}{\lambda_1 + \lambda_3 - \lambda_2}. \quad (2.45c)$$

From these dependencies the intrinsic ellipticities ϵ_i were obtained as

$$\epsilon_1 = 1 - \frac{c}{b} = 1 - \sqrt{\frac{\lambda_1 + \lambda_2 - \lambda_3}{\lambda_1 + \lambda_3 - \lambda_2}}, \quad (2.46a)$$

$$\epsilon_2 = 1 - \frac{c}{a} = 1 - \sqrt{\frac{\lambda_1 + \lambda_2 - \lambda_3}{\lambda_3 + \lambda_2 - \lambda_1}}. \quad (2.46b)$$

This way the ellipticities are set up to be $\epsilon_1 \leq \epsilon_2$ and correspond to the ellipses with minimum and maximum ellipticities: $\epsilon_1 = \epsilon_{min}$ and $\epsilon_2 = \epsilon_{max}$. It also holds the advantage of keeping the ellipses in a geometric configuration perpendicular to each other, which in turn is a way to evaluate the prolateness, oblateness, or triaxiality of the system. For $\epsilon_1 \approx 0$ and $\epsilon_2 > 0$ the system is prolate, for $\epsilon_1 \approx \epsilon_2 > 0$ the system is oblate and for $\epsilon_2 > \epsilon_1 > 0$ the system is triaxial.

3. Unperturbed Radial Orbit Instability

3.1. Dynamical Evolution

The purpose of the following chapter is to visualise the dynamical evolution of both density profiles (Hernquist and Plummer, see Sec. 1.3) as they undergo unperturbed ROI. This is done by plotting the simulations that show the most elliptic final states for each the Plummer and Hernquist density profile in position- and phase-space and in the density distribution respectively. Those simulations are "P-0,25" for the Plummer profile and "H-0,25" for the Hernquist profile. Parameters for these simulations can be found in Sec. III.2.1. The beforementioned concept of ellipticity will be discussed in Sec. 3.2.

3.1.1. Plummer Setup

Fig. 3.1 shows the initial condition of the system. Both the position-space and the density distribution are that of an ideal Plummer sphere, only the phase-space shows deviations from an equilibrium system which will lead to the imminent collapse. By rescaling the equilibrium velocities in the way explained in section 2.3.1, the radial velocities are reduced. This is indicated in phase-space by a cigar-like distribution instead of the cone-like distribution of a system in equilibrium. It is important to note that in this configuration the velocity dispersion is still very much random and the signs of the radial velocities are both positive and negative, so particles would move inward and outward. This is, however, only an artefact of the way the initial conditions were set up.

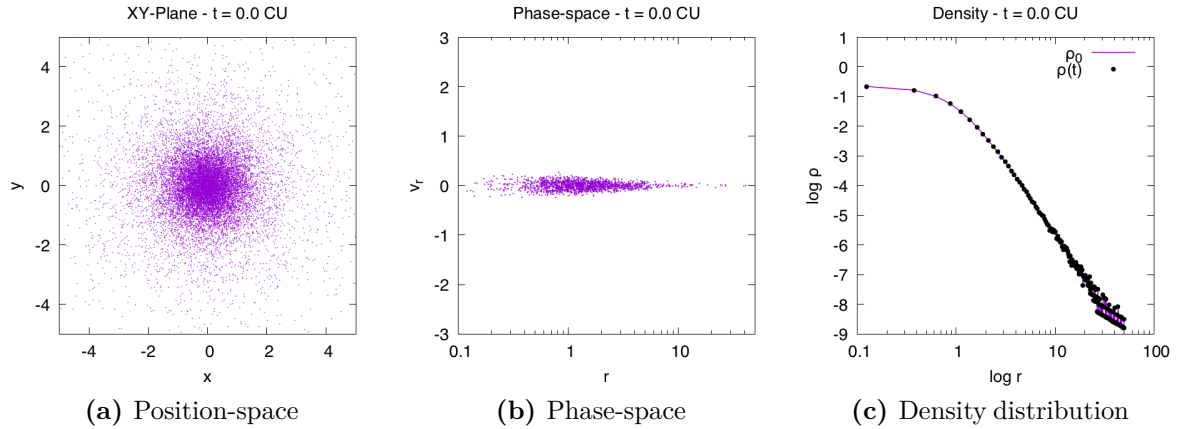


Figure 3.1.: Plummer-profile: Initial condition

As soon as the simulation is started, the potential energy dominates the dynamical evolution and the system collapses. This can be seen in all of the three plots in Fig. 3.2. The position-space shows a compact core, which is more evident in the sudden rise in density at small radii (Fig. 3.2 c). In phase-space the signs of the particles are predominantly negative, which corresponds to an inward motion.

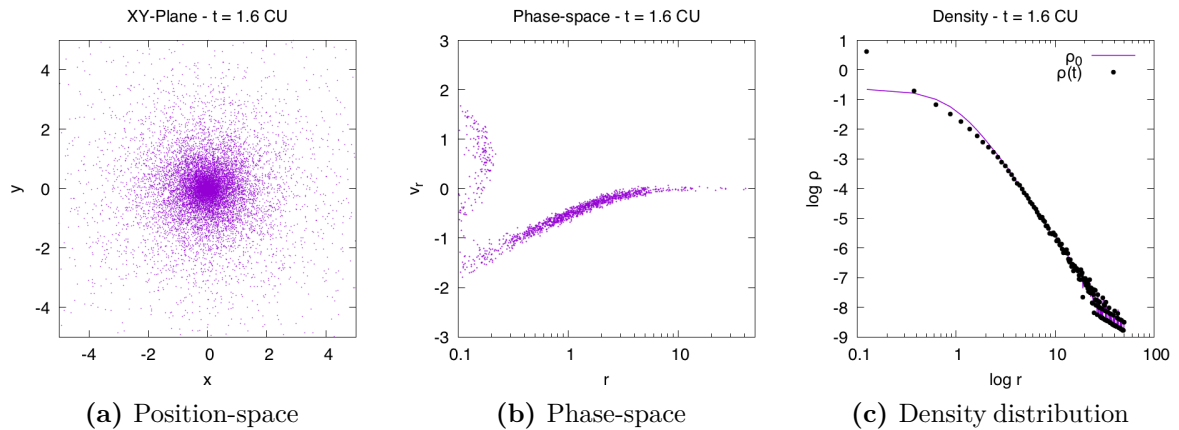


Figure 3.2.: Plummer-profile: At the First infall

Once the particles have passed the center, the sign becomes positive as they begin to move outwards again. This leads to a kind of spiral-shape in the phase-space diagram, hints of which first occur in Fig. 3.2 and become more evident in Fig. 3.3.

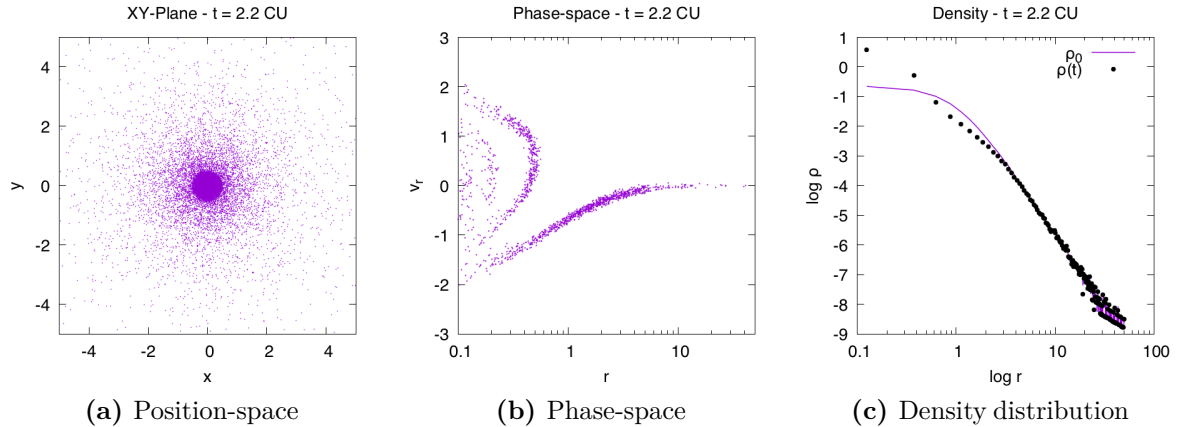


Figure 3.3.: Plummer-profile: After the turnaround point

These twirls in phase-space are accompanied by outwards moving shells in position-space and are especially evident in the density distribution where they move outwards in density-waves as can be seen in Fig. 3.4 a) and c) respectively. It is important to note that at this point in the evolution, the system still appears to be spherically symmetric. This is only a very short-lived state however. The system undergoes a rapid change in ellipticity at this time, as can be seen from the high increase of ϵ_2 in Fig. 3.9 b). This rapid growth of ellipticity shows how violently the onset of ROI works on the system.

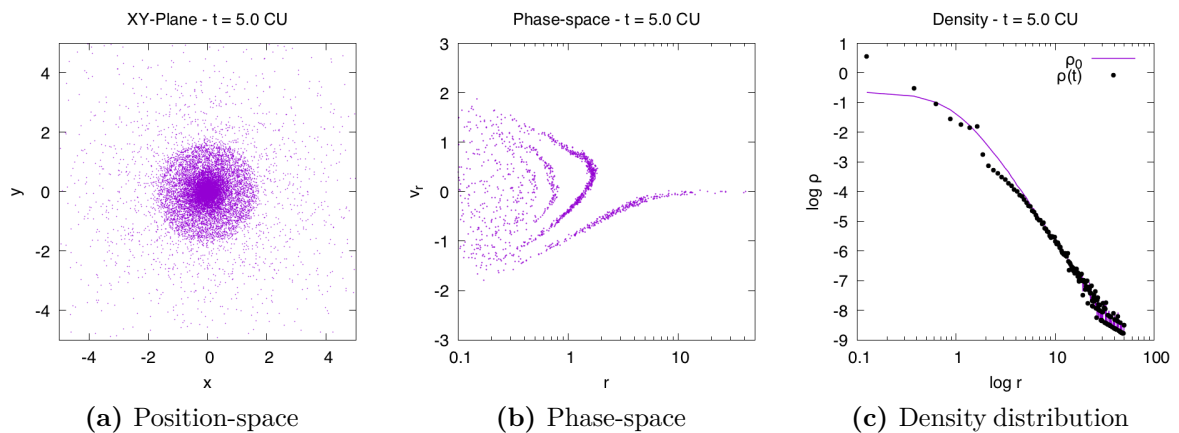


Figure 3.4.: Plummer-profile: Density-waves form

At $t = 10$ in code-units, corresponding to 5 Myrs in physical units, the core of the system has reached its maximum ellipticity which will slowly decline over the remainder of the simulation (Fig. 3.9 b)). The outward motion of the density waves becomes more prominent in Fig. 3.5, but the central region keeps its peak in density. Phase-space shows some interesting behaviour, as the previously smooth spirals are compressed and

show saw-tooth-like shapes. This inhomogeneity in phase-space is evidence for the inherit instability.

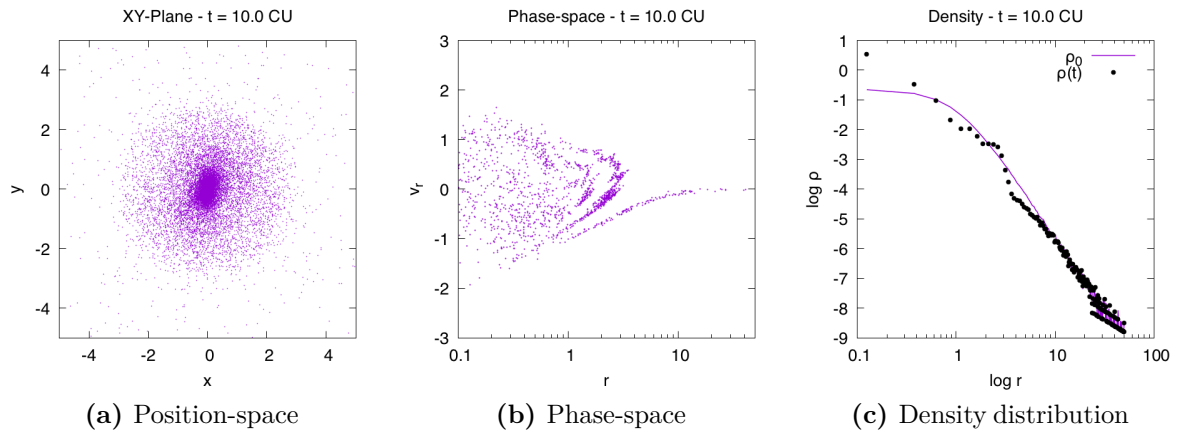


Figure 3.5.: Plummer-profile: The density waves move outwards

Fig. 3.6 shows the system at $t = 25$. In position space even the outer regions of the system have undergone ROI and have taken on an elliptical shape. Phase-space shows evidence of a beginning phase-mixing. Phase-mixing describes how, after the system has initially collapsed and stars find their new orbits in the changed energy regimes, the spiral shapes in the phase-space diagram seem to disappear. In reality the spiral still exists, only the space between the arms becomes smaller, as the stars follow their new orbits in different orbital periods until they are undistinguishable by eye. The initial conditions could be reconstructed by analysing the phase-space density, as long as the radial velocities can be measured at sufficient accuracy.

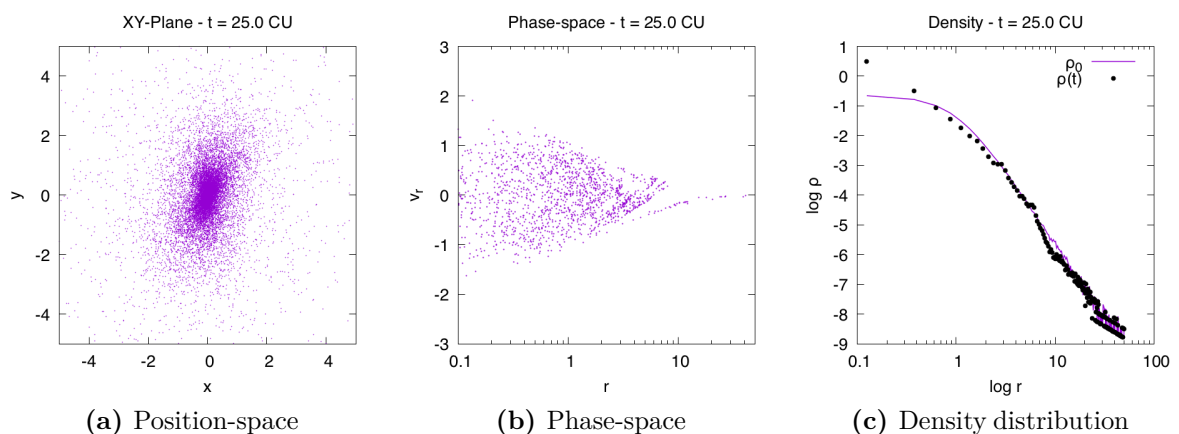


Figure 3.6.: Plummer-profile: The beginning of phase-mixing

The result of phase-mixing becomes more evident in fig 3.7. Here the inner regions seem

to have no distinct structure, only the outer regions at around $R \approx 10$ still have clear groups of particles moving on similar paths in phase-space. MacMillan et al. (2006) call this effect "Virialisation from the inside out". The density waves have proceeded to move out to that region as well. This effect also levels out some of the ellipticity in the outer regions, as movements start to become more random again.

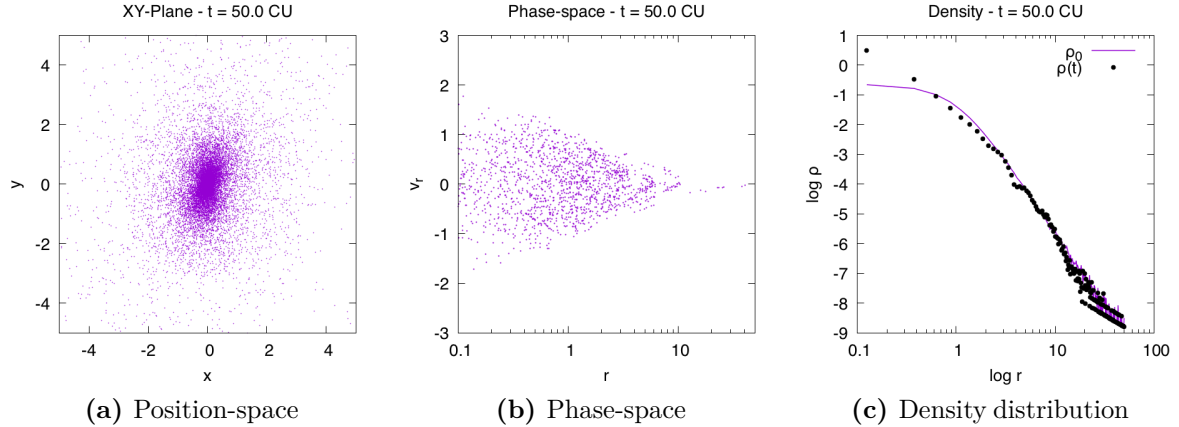


Figure 3.7.: Plummer-profile: The inner shells appear phase-mixed

Fig. 3.8 shows the final state of the evolution. The position-space still shows a very elliptical shape of the inner regions, while the outer regions have become more spherical. Phase-space appears completely mixed, except for the outermost region where some of the initially grouped trajectories can still be distinguished. It shows the beforementioned cone-like shape of an equilibrium system, where the boundaries of the shape are normally defined by the escape-velocity $v_{esc}(r)$ of the system at that radius. It appears as if the escape velocity at these radii should be higher than the cutoff, which would indicate that not all of the available phase-space is filled. Analysing this question should be done in future studies.

The best evidence for the previous collapse can be found in the density distribution. The two density waves can be observed on the outskirts of the system and the drop in density starting from about $\log(r) \approx 11$ is also fairly evident. Due to the finite particle numbers in the simulation needs to be considered that small changes in the number of particles per density-shell lead to high fluctuations in the density profile. As the density in this region is of the order $\log(\rho) \approx -8$ just a single particle entering or leaving the shell in which the density is calculated can have a high impact on the density in that shell.

Fig. 3.9 gives an overview of some of the intrinsic features of the system and how they evolve over time. Fig. 3.9 a) shows the evolution of the half mass radius (HMR). The plot clearly displays the initial collapse and the following pulsation of the central region, which leads to the waves in the density profile. It is also important to note the correlation between the fluctuation of the HMR in Fig. 3.9 a) and the fluctuation of the virial ratio η_{vir} in Fig. 3.9 c). This behaviour is to be expected: As the system moves towards a new equilibrium-state with $\eta_{vir} \rightarrow 1$ the orbits of the stars begin to stabilise. This in

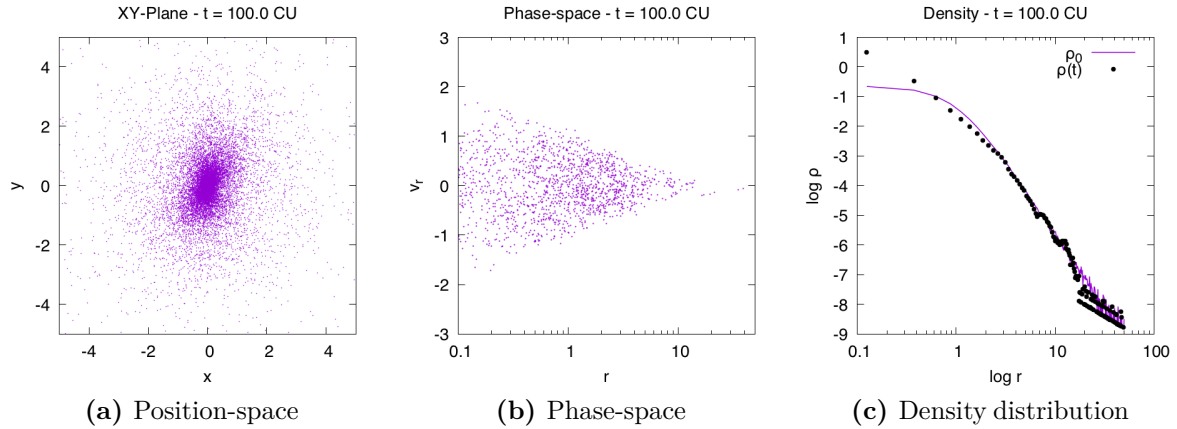


Figure 3.8.: Plummer-profile: End of the simulation

term leads to a constant exchange of stars in the inner regions, which can be observed in phase-space as the beforementioned phase-mixing. Phasemixing stabilises the density profile which again leads to a more and more constant HMR. The evolution of ellipticity is shown in Fig. 3.9 b). While the initial condition is fairly spherical with an ellipticity of $\epsilon_{1,2} \approx 0$, it rapidly evolves towards its final prolate shape with $\epsilon_2 \approx 0.5$ and $\epsilon_1 \approx 0$. This is in accordance with the violence of such dynamical changes predicted by Lynden-Bell (1967). The slight decline of ϵ_2 over the remainder of the simulations will be cause for discussion in Sec. 3.3. Since particles scatter each other through their random motion the system will slowly become less elliptical and relax to a new spherical distribution within the relaxation timescale discussed in section 2.5.

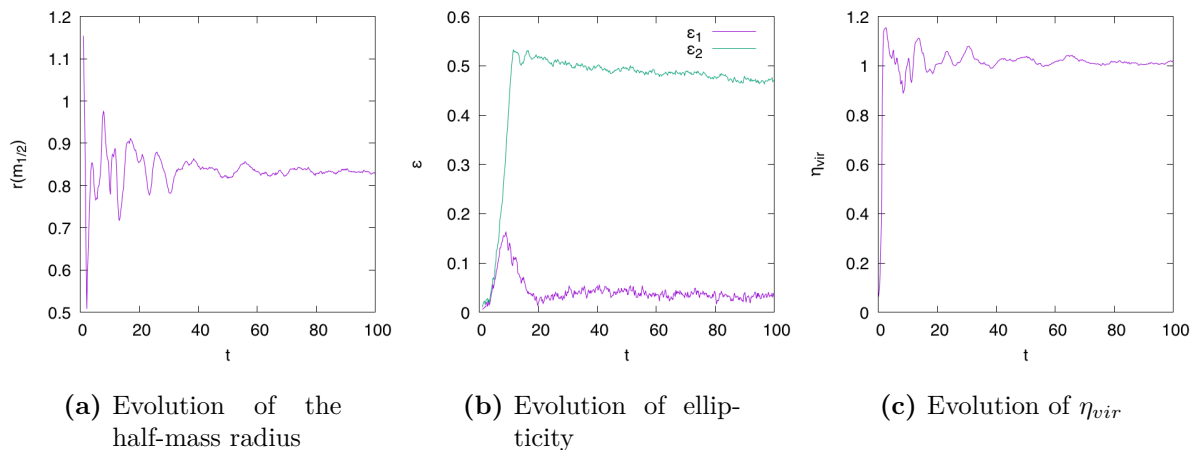


Figure 3.9.: Evolution of HMR, ellipticity and η_{vir}

3.1.2. Hernquist Setup

The same experiment is done with an initial Hernquist sphere. The figures for this setup can be found in the appendix in Sec. III.1.1. Figures III.1 through III.9 show the same steps in the Hernquist evolution. The initial conditions are displayed in Fig. III.1 and appear to be an ideal Hernquist density distribution. Only the phase-space is compressed in the same way as for the Plummer sphere case (see Fig. 3.1). The first difference between the Hernquist and Plummer setups can be seen in Fig. III.2: Since the core of the Hernquist profile is a lot denser than the core of the Plummer profile, the freefall time (see Eq. 2.37) of the innermost particles is smaller. This leads to a faster collapse of the core and the point at which the first stars start to move outwards again is reached after only $t = 1.0$ in contrast to $t \approx 1.6$ in the Plummer case. For the same reason in the Hernquist profile case more particles have passed the center of the system, which can be observed as four instead of three spiral arms in phase-space at $t = 2.2$ (Fig. III.3). The rest of the evolution appears rather similar to that of the Plummer system, with density waves moving outwards (Fig. III.4), evidence for the instability in phase-space (Fig. III.5) and the beginning of phase-mixing (Fig. III.6). One major difference between the profiles is that the outer regions of the Hernquist profile catch up to the ellipticity a lot slower than those of the Plummer profile. Fig. III.6 shows the highest ellipticity in the outer regions of position-space, while at the same time ($t = 50.0$) in the Plummer profile the outer regions have already started to lose their elliptical shape. At the end of the simulation another difference can be observed: phase-mixing seems to take longer in the Hernquist system. While the Plummer phase-space appears mostly homogeneous, the Hernquist phase-space shows some clear structure of the initial spirals, even at small radii.

3.2. Ellipticity

A key question of this work was to study the evolution of the central, bar-like structure that develops during the ROI. The matter in question was, if there is a point at a certain $\eta_{vir,crit}$ where a sudden onset of ROI can be observed. The follow-up question of course was how the geometric evolution progresses after that point, whether it grows rapidly, or slowly, whether the resulting ellipticity converges at some point, if it keeps growing or declines again.

Fig. 3.10 and 3.12 show the ellipticity within the HMR plotted against decreasing η_{vir} of the initial condition for the Plummer and Hernquist case, respectively. The plots are divided into three segments to account for changes in the x-axis. In order to portray the steep rise in ellipticity for $10^{-2} < \eta_{vir} < 0.2$, the middle segment zooms into that range of the x-axis. The right segment changes the x-axis to a logarithmic scale to account for the bigger stepsize between the original χ -factors. All values for the ellipticities were taken from the end of the simulations at $t = 100$. Following Fig. 3.9 there would also have been the option to take the value of maximum ellipticity, as ϵ_2 declines slightly over the time of the simulation. This approach was discarded, because at that state the system is far

from virial-equilibrium, which seemed less favorable. Therefore all ellipticities discussed in Sec. 3.2.1 and Sec. 3.2.2 are the final ellipticities of the systems. Problems arising with this definition will be discussed in Section 3.3.

3.2.1. Plummer-Profile

Figure 3.10 shows the evolution of ϵ for the Plummer profile. For the equilibrium setup the ellipticities are very low, hence the system is approximately spherical. There is a slight tendency towards triaxiality, but at these small values for ϵ they could also be caused by random fluctuations. As the system is dynamically cooled down and η_{vir} decreases, the values for $\epsilon_{1,2}$ vary slightly around the ones for the equilibrium system, but stay fairly constant until $\eta_{vir} = 0.16$. Once η_{vir} passes 0.16 the ellipticity ϵ_2 increases drastically until it reaches a temporary maximum at $\eta_{vir} \approx 0.12$. In the same range, while ϵ_2 increases, ϵ_1 stays close to zero, which indicates the prolate shape that is one of the key features of ROI. As the system cools down even more, ϵ_2 decreases again and hits a temporary minimum at $\eta_{vir} \approx 0.1$. Since ϵ_1 increases at the same time, the system becomes more triaxial in that process. This sudden dip in ellipticity is quite intriguing as it consists of three datapoints with higher resolution than most of the other simulations, but with the same resolution as their neighboring datapoints with higher ellipticity ϵ_2 and lower triaxiality. All in all the dip consists of four datapoints that are significantly lower than the surrounding ellipticity values.

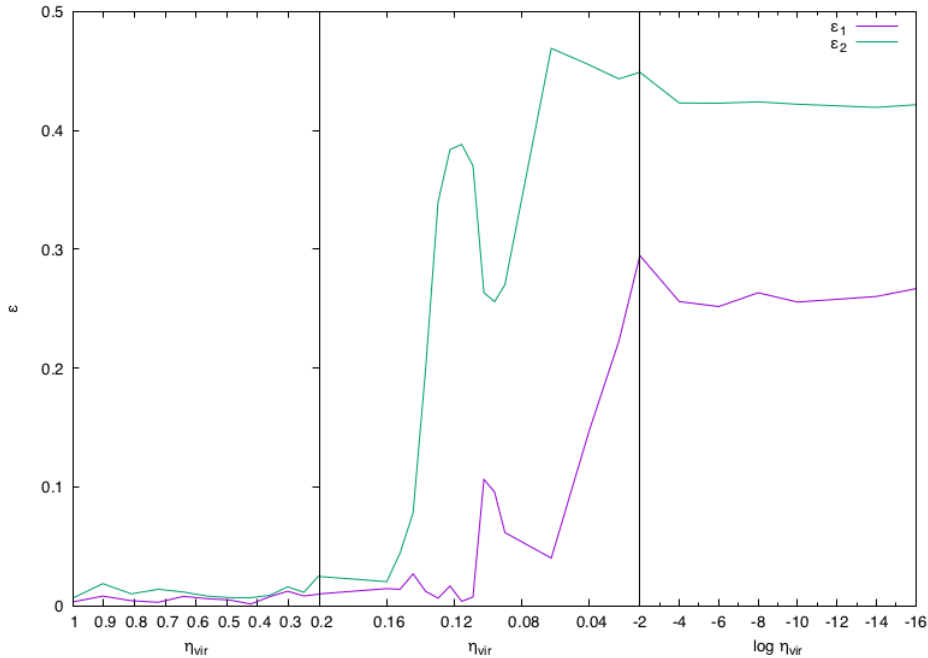


Figure 3.10.: Evolution of ellipticity with decreasing η_{vir}

Looking at the ellipticity evolution in the simulations where the dip occurred (see Fig. 3.11 for one example) one can see that the system reaches an initial maximum at $\epsilon_2 \approx 0.5$, which would fit the expected curve, but then drops significantly over the rest of the simulation, while ϵ_1 grows within the last 10% of the simulation time. This is especially unanticipated since the system is almost in perfect virial equilibrium, as Fig. 3.11 b) shows.

To address this issue, the impact of resolution on the evolution of ellipticity will be discussed in Sec. 3.3.

After $\eta_{vir} \approx 0.08$, ellipticity ϵ_2 increases again and reaches the maximum of all simulations ($\epsilon_2 \approx 0.48$) at $\eta_{vir} \approx 0.06$. At this point the system is also almost perfectly prolate again, as ϵ_1 decreases in that range. For $\eta_{vir} < 0.06$ the systems become more and more triaxial until they reach constant values of $\epsilon_1 \approx 0.42$ and $\epsilon_2 \approx 0.26$ at $\log(\eta_{vir}) = -4$.

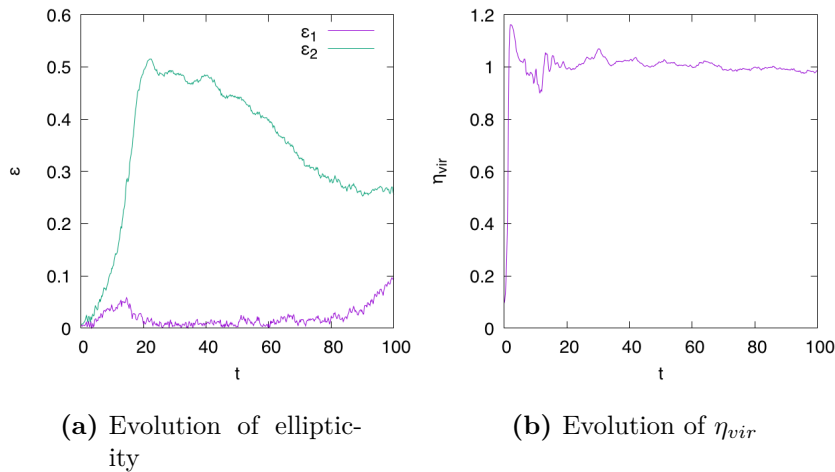


Figure 3.11.: Evolution of ϵ and η_{vir} in the system "P-0,31"

3.2.2. Hernquist-Profile

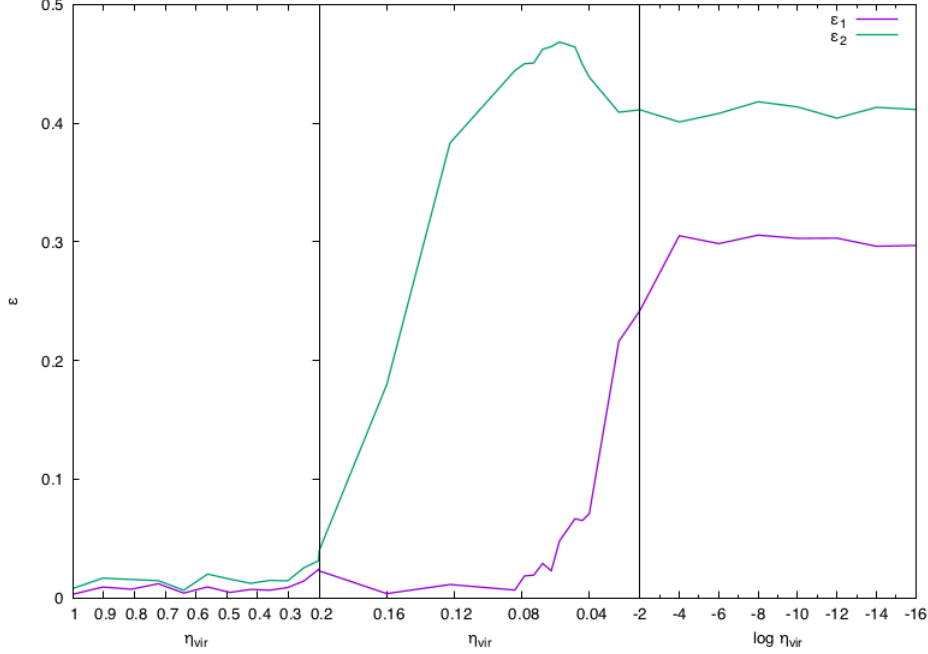


Figure 3.12.: Evolution of ellipticity with decreasing η_{vir}

As Fig. 3.12 shows, the Hernquist systems behave a little different from the Plummer systems. For one the onset of the ROI starts a little earlier, at $\eta_{vir} \approx 0.2$. The ellipticity ϵ_2 proceeds to grow as the systems become dynamically colder and reaches the same value as the Plummer system at $\eta_{vir} \approx 0.12$. This in term means that the growth in ϵ is less steep and therefore the onset of ROI is less violent. Unlike the Plummer systems there is no dip in the evolution of ϵ_2 , which raises the question if the Hernquist systems are more stable and keep the shape induced by ROI longer. This will be discussed in more detail in section 3.3. Until $\eta_{vir} \approx 0.08$ the systems are almost perfectly prolate. As η_{vir} passes 0.08 the systems become more triaxial until they stay fairly constant after $\log(\eta_{vir}) = -4$. Much like in the Plummer case, the growing triaxiality and the increase in ϵ_1 is accompanied by a decrease in ϵ_2 . The difference in this triaxial regime is how the triaxiality is reached: While in the Plummer case the system first reaches a prolate phase, which becomes more triaxial over the remainder of the simulation for sufficiently small values of η_{vir} (see Fig. 3.11 and Fig. 3.15), the Hernquist system does not undergo a change in shape, but reaches its triaxial configuration faster and without an intermediate prolate phase (see Fig. 3.13).

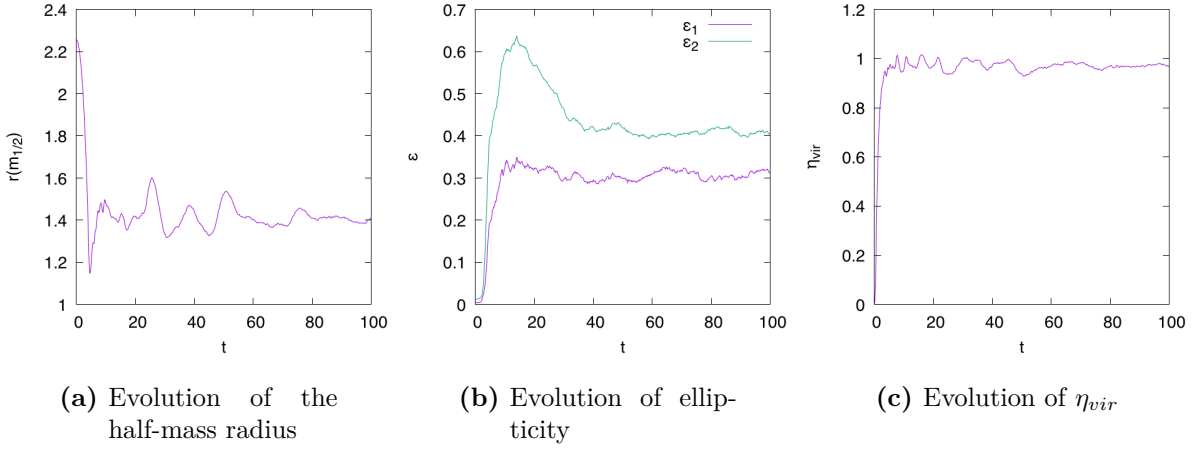


Figure 3.13.: Evolution of HMR, ellipticity and η_{vir} in the Hernquist system "H-e-4", see Sec. III.2.1 for parameters.

3.3. Impact of resolution

To discuss the impact of resolution on the final ellipticity, high-resolution simulations were performed. Since these simulations are computationally very expensive, only a few of them were conducted and only at prominent values of η_{vir} . Resolution is in this case referring to a smaller timestep size and a smaller softening length, rather than a higher number of particles. For the Plummer profile those values were chosen to be in the vicinity of the observed dip, to estimate if the dip is caused by numerical effects or not. For the Hernquist profile the values were chosen to observe a shift in the onset of ROI, or the onset of the triaxiality, hence less tests were performed. The parameters of these simulations can be taken from Sec. III.2.1 in the appendix.

3.3.1. Plummer profile

Fig. 3.14 shows the previous $\epsilon_{1,2}$ evolution overplotted by the tests with increased resolution. It shows that with increasing resolution the triaxiality of the systems also increases. The value for ϵ_2 at $\eta_{vir} = 1.156 \cdot 10^{-1}$ also indicates that the dip in ellipticity is not of numeric nature. As the value is higher than next value at $\eta_{vir} = 1.024 \cdot 10^{-1}$ the dip seems to occur even in the high-resolution simulations.

Looking at the evolution of ellipticity over the time of the simulation in Fig. 3.15, the same tendency can be observed. At high resolutions and with decreasing η_{vir} , the timescale in which the system leaves its prolate shape and develops a triaxial configuration shrinks. While at $\eta_{vir} = 1.156 \cdot 10^{-1}$ the value of ϵ_1 stays fairly constant at $\epsilon \approx 0$ and the value of ϵ_2 decreases constantly, the resulting shape is still prolate. For smaller values of η_{vir} the decrease of ϵ_2 stops after proceedingly shorter times and after a short increase, a constant value for ϵ_2 is reached. Complementary, the value of ϵ_1 increases until it reaches

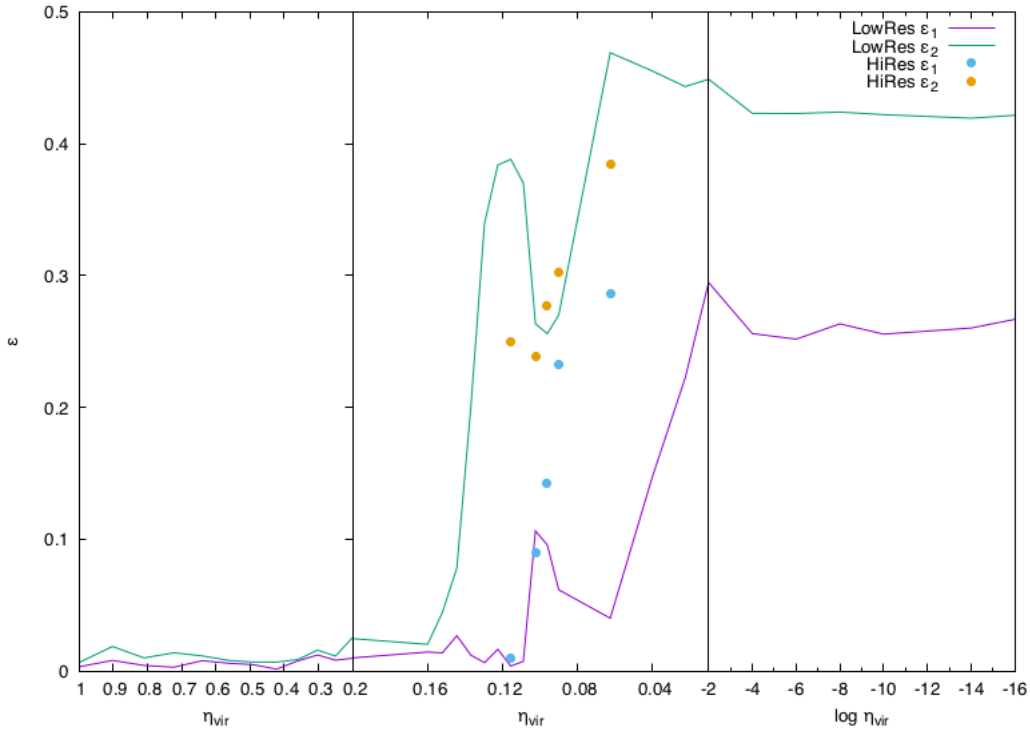


Figure 3.14.: Resolution-impact on Plummer-profile

a constant value and causes the resulting shape to be triaxial. This indicates that the onset of triaxiality is shifted to dynamically warmer regimes.

Acknowledging these results, the resolution for the general simulations is nevertheless kept at lower values. This decision was made for three reasons: First, the higher resolution only shifts the onset of triaxiality, while the values for ϵ_2 stay fairly close to those of the lower resolution simulations. Even more so, the tendency of the behaviour of ϵ_2 stays the same, which indicates that the final 2-dimensional shape of the bar is not influenced by the resolution as much, as the 3-dimensional configuration. Following Fig. 3.15 that behaviour of ϵ_1 can be estimated and therefore included in the conclusion. The second reason was that the high-resolution simulations were so computationally expensive that obtaining a high resolution in datapoints for η_{vir} would have been impossible, but that was the key question of this work. Third, the high-resolution simulations of the Hernquist profile show less divergence from the low-resolution ones, as will be seen in the next chapter. Hence, to ensure a comparability between both profiles, the resolution was kept at the lower values.

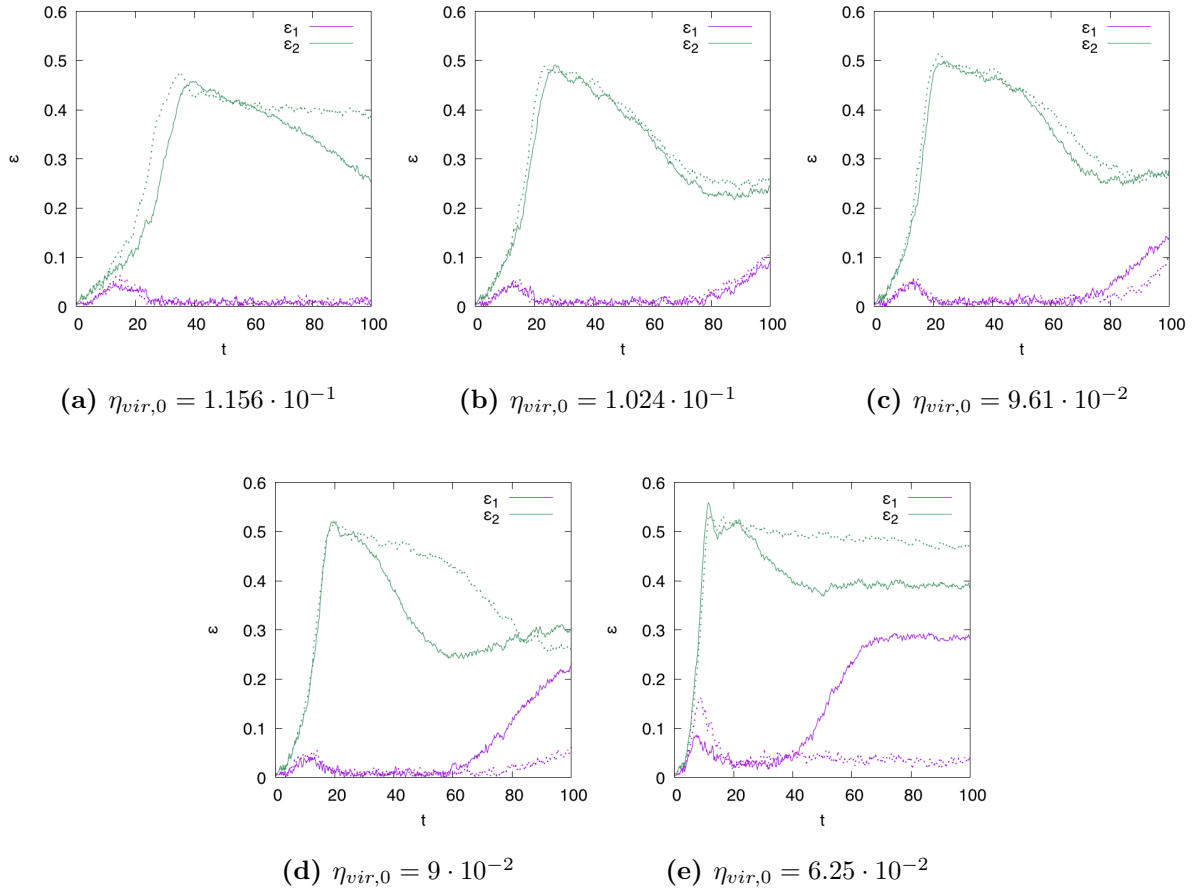


Figure 3.15.: Evolution of ellipticities. Solid lines: high-resolution simulations. Dashed lines: low-resolution simulations.

3.3.2. Hernquist profile

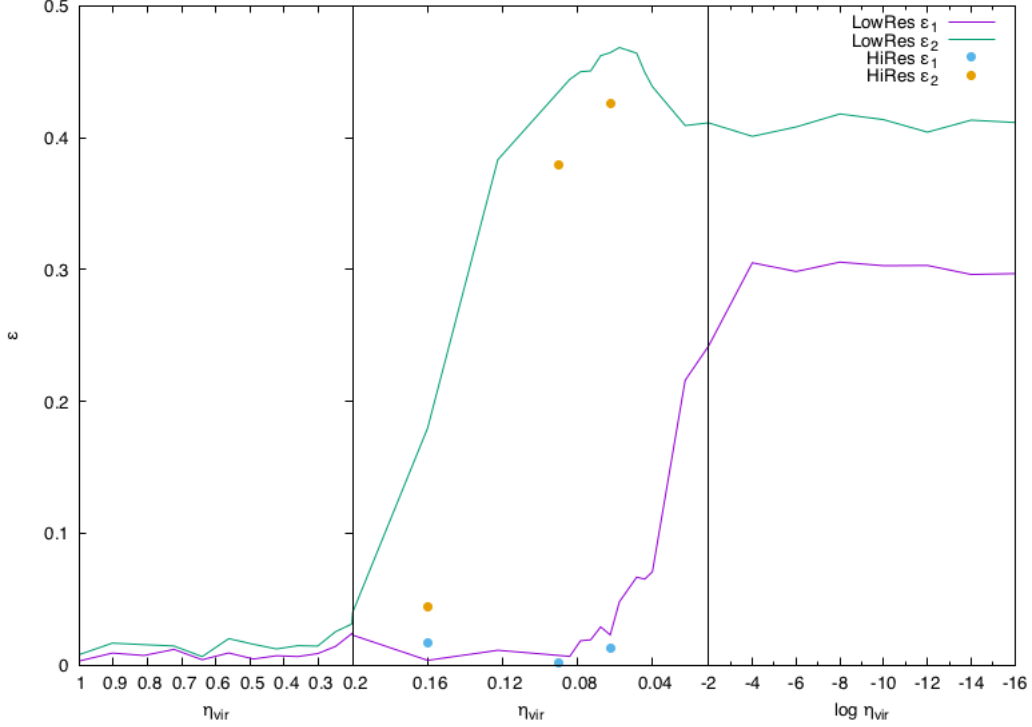


Figure 3.16.: Resolution-impact on Hernquist-profile

In contrast to the simulations with the Plummer profile, a higher resolution in the Hernquist setups does not seem to shift the beginning triaxiality towards dynamically warmer regimes. Instead the ellipticity of ϵ_1 stays very close to that of the low-resolution simulations and therefore the systems where ROI can be observed keep their prolate shape over the entire time of the simulation. For the systems with $\eta_{vir} = 0.09$ and $\eta_{vir} = 6.25 \cdot 10^{-2}$ the values for ϵ_2 also stay almost the same as in the low-resolution simulations. The only significant difference is the shift of the onset of ROI. In the low-resolution tests the system with $\eta_{vir} = 0.16$ shows a higher value of ϵ_2 , therefore the impact of ROI is apparent already at this value of η_{vir} , while in the high-resolution simulation the system remains spherically symmetric. The high resolution tests indicate that a smaller timestep-size shifts the onset of ROI to dynamically colder regimes with a shift-phase of $\Delta\eta_{vir} \approx 0.04$. Fig. 3.17 shows the evolution of ellipticity in the individual systems. It indicates that once the systems have undergone ROI, they stay almost constant and keep their prolate shapes. In contrast to the Plummer systems there seems to be no second change in shape over the remainder of the simulations.

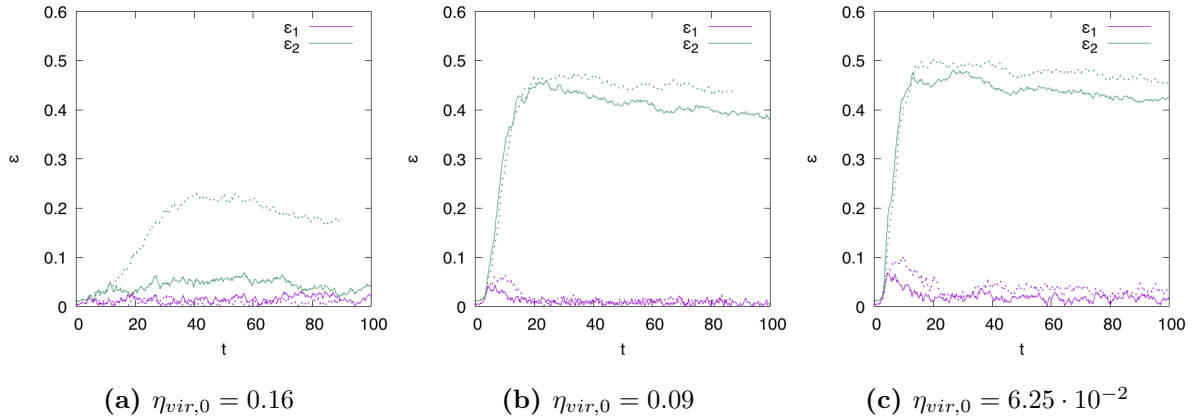


Figure 3.17.: Evolution of ellipticities. Solid lines: high-resolution simulations. Dashed lines: low-resolution simulations.

It would be of interest to perform more simulations with even higher resolutions to check if the onset of ROI is shifted even further to dynamically colder regimes. In the same process it would be interesting to go for longer run-times to see if the Hernquist profile also undergoes a second change of shape, like the Plummer profile, only at later stages of the evolution. Both these questions will have to be discussed in future work, as the run-times for these simulations would exceed 1000 cpu-hours with the given code.

4. Perturbed Radial Orbit Instability

In contrast to the previous chapter, the purpose of this chapter is to study the evolution of ROI under not-ideal conditions. For this reason different systems with a rigid body rotation and a compact central mass at the center of the system were set up in the way described in Sec. 2.3.2 and Sec. 2.3.3, respectively.

4.1. Rotation

The first disturbance to be tested is an addition of rotational velocity to the initial conditions of the Plummer- and Hernquist spheres. Since both the anisotropy-parameter (eq. 1.4) used by Bellovary et al. (2008) and the russian stability criterion (eq. 1.1) suggestes by Polyachenko and Shukhman (1981) rely on the proportion of radial- to tangential velocity, it is reasonable to try and test the boundaries of that assumption. The setup was done as described in Sec. 2.3.2. A table with all conducted tests can be found at Sec. III.2.2 in the appendix.

4.1.1. Plummer Setup

The result of these tests can be seen in Fig. 4.1. Both plots show equal behaviour for ϵ_1 and ϵ_2 in the dynamically cold regime (i.e. $\eta_{vir} \ll 1$), which is to be expected. Because of the way the system is set up, as it is artificially cooled down by multiplying the velocities with a constant factor $\chi < 1$, all velocities scale down by the same factor. Since the rotational velocity is added to the particle velocities before they are scaled down, the additional rotation becomes too small of a factor to have a real influence on the dynamical evolution. This seems to be the case for ϵ_2 in the setups with an η_{vir} colder than $\eta_{vir} = 4 \cdot 10^{-2}$. The dynamically warm regime shows no change under different values for Ω either.

Only the ϵ_1 values in the systems with intermediate rotation show lower ellipticities at $\eta_{vir} = 0.09$.

To illustrate this problem fig. 4.2 displays a direct comparison between the ellipticities of the rotation setups and those of the undisturbed setups. This way it becomes more apparent that the deviations between the non-rotating initial conditions are in general very small. Only the unusual dip in the ϵ_2 ellipticity evolution is altered significantly for two values of Ω , namely $\log(\Omega) = -4$ and $\log(\Omega) = -3$. Since these two values of Ω are the minimum and maximum values of Ω , the correlation between rotation and decrease in

ϵ_2 and increase in ϵ_1 remains questionable. Following equations 1.1 and 1.4, for a reliable evidence of an additional effect, the ellipticity should correlate in some way with Ω . To get an impression of the evolution of the ellipticities, they are plotted against the ideal system in Fig. 4.3.

This again shows that there is no clear correlation. The initial maxima of the ϵ_2 value in each simulation are essentially the same, only the evolution of the ellipticities diverge at around $t = 40$. Since neither this point of divergence, nor the resulting ellipticities correlate with Ω it is highly likely that this change in ϵ_1 is not caused by the rotation.

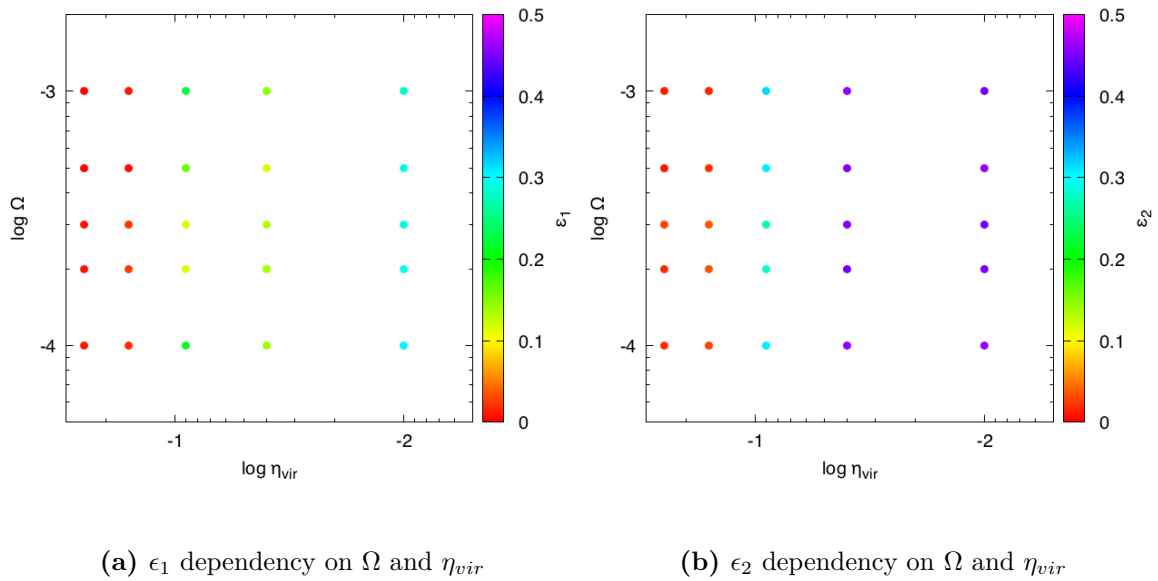


Figure 4.1.: Evolution of the ellipticity under different conditions of rotational velocity Ω and virial coefficient η_{vir} . Both Ω and η_{vir} are displayed logarithmically, while the values of ϵ are color-coded.

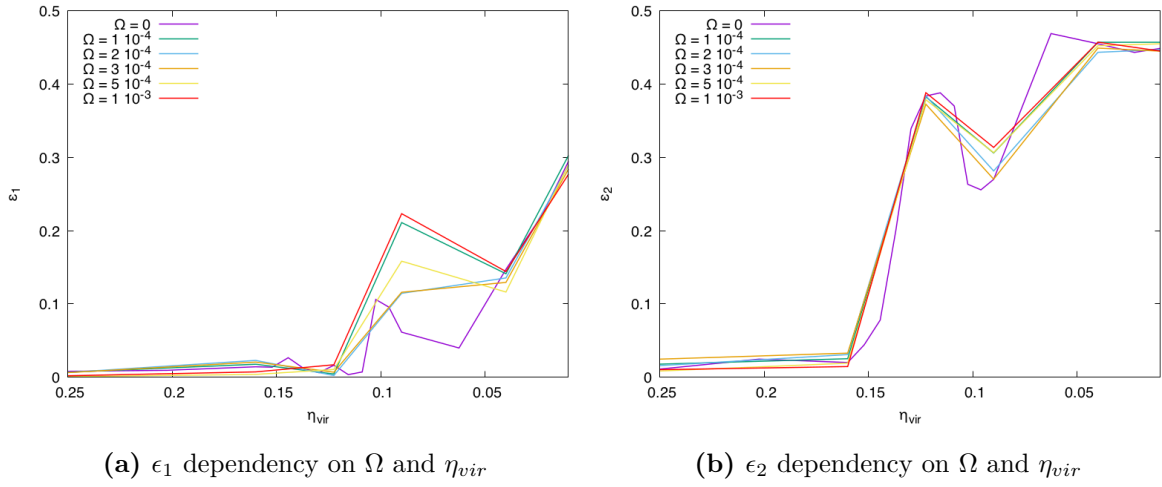


Figure 4.2.: Comparison of the ellipticities to those of the systems without rotation.

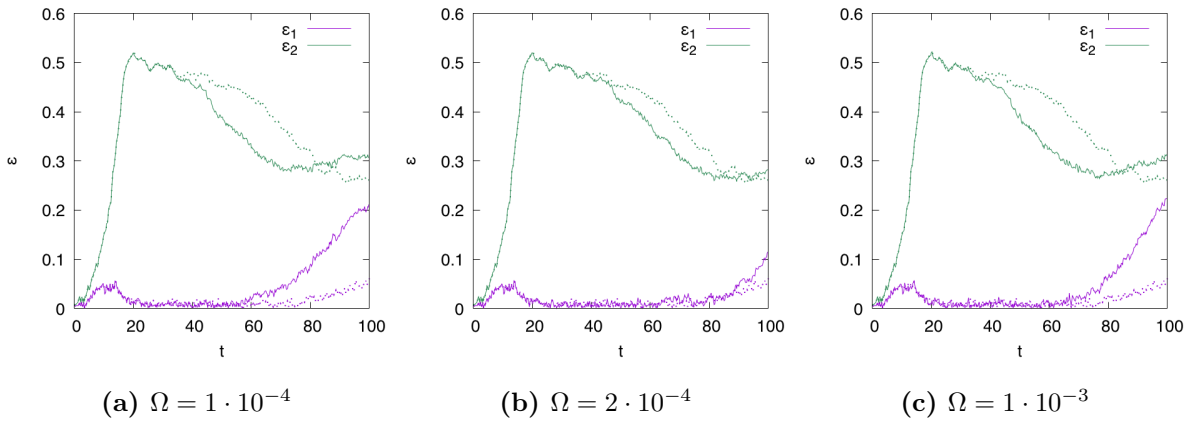


Figure 4.3.: Evolution of ellipticity in the systems with $\eta_{vir} = 0.09$. Solid lines: System with rotation. Dashed lines: System without rotation.

4.1.2. Hernquist Setup

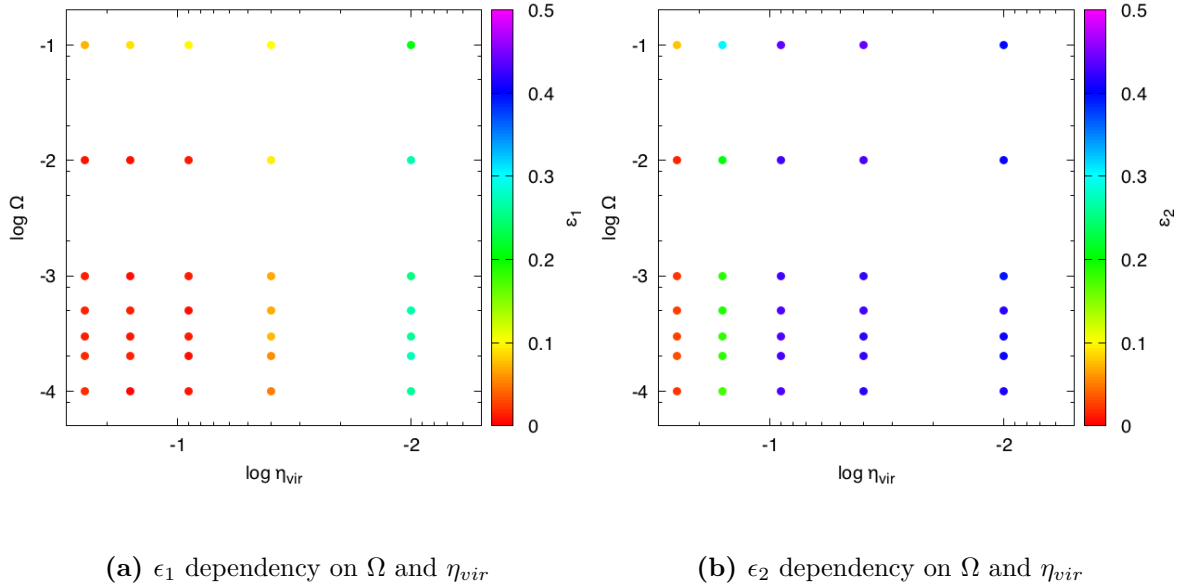


Figure 4.4.: Evolution of ellipticity under different conditions of rotational velocity Ω and virial coefficient η_{vir}

In contrast to the Plummer spheres there is almost no evidence for an impact of rotation on the development of ROI in the Hernquist spheres at the same values of Ω that were used for the Plummer case, namely $10^{-4} \leq \Omega \leq 10^{-3}$.

There seems to be no influence on the development of ROI and remarkably not even on the evolution of ϵ over the time of the simulation, as it can be seen in the Plummer case. It seems evident that the additional rotational velocity is too small to play a role in the Hernquist systems. This could be caused by the profile itself: Since the rotational velocity v_ϕ scales with the distance to the rotational axis and the density of the Hernquist profile decreases quite rapidly, there are not enough particles in the zone of the profile that is close enough to the center to have a major impact on the first collapsing stars and still far enough from the center to get sufficient additional velocity from the rotation.

To account for this problem, additional values for Ω were tested to stretch the range of Ω over 4 orders of magnitude. As can be seen in Fig. 4.5, even these very high values of Ω show no sign of significantly changing the impact of ROI in the dynamically colder setups. It seems that only the additional rotation with $\log(\Omega) = -1$ increases the ellipticity in the dynamically warmer setups, so the onset of ROI is shifted. Since the rest of the values fit the unperturbed case very well this also means that the slope of the onset is decreased, hence the growth in ellipticity starts earlier, but progresses slower.

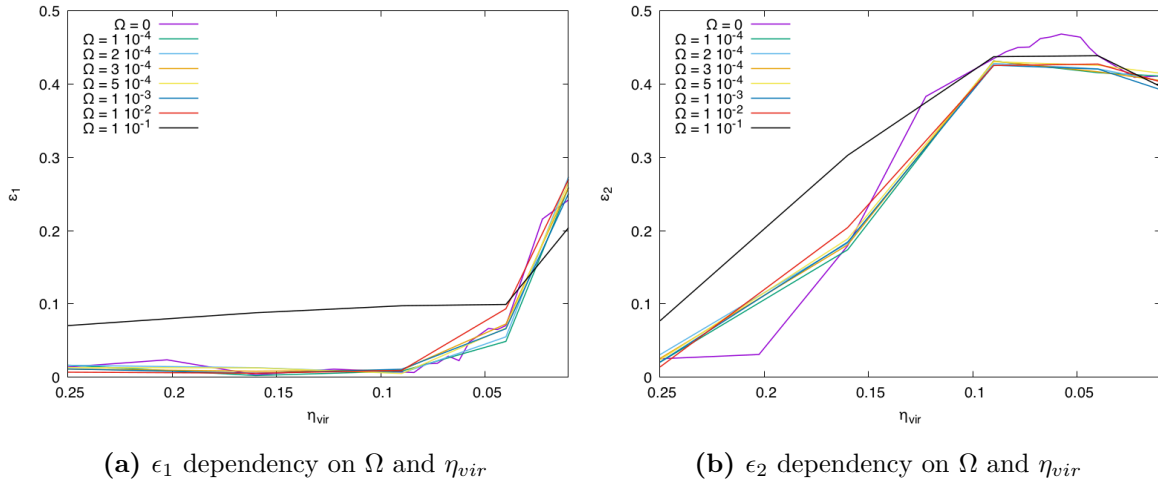


Figure 4.5.: Evolution of ellipticity under different conditions of rotational velocity Ω and virial coefficient η_{vir}

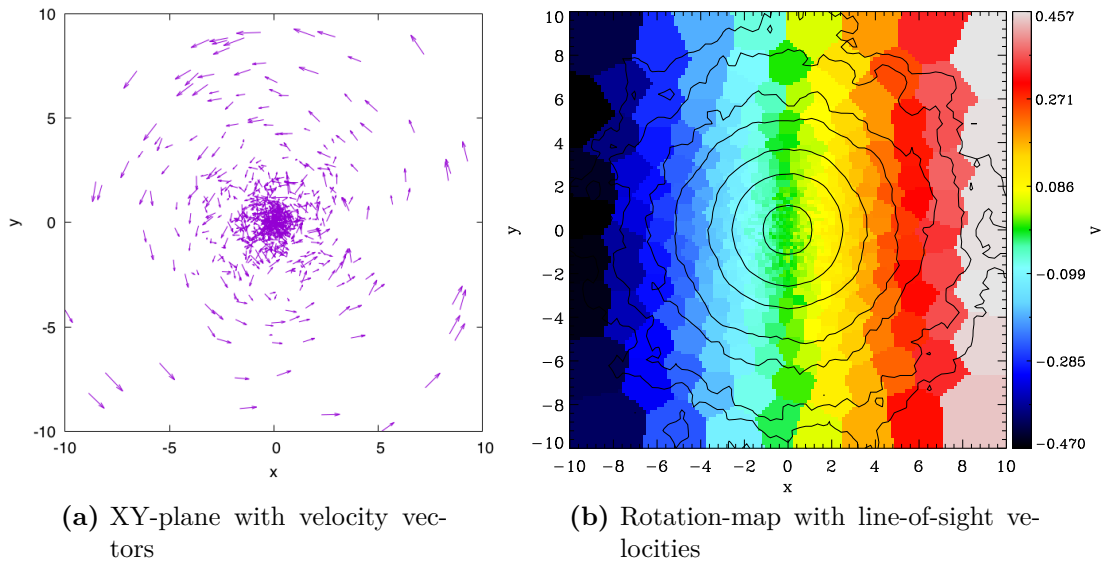


Figure 4.6.: Plot of rotational velocities in the initial conditions

To visualise the rotation setup, Fig.4.6 shows the initial condition of the system with $\log(\Omega) = -1$ and $\eta_{vir} = 0.25$, which showed the highest values for ϵ_2 , compared to the unperturbed case. As can be seen in both plots of Fig. 4.6, there is a distinct counter-clockwise rotation of the system. Fig. 4.6 shows that the outer regions are dominated by rotational velocity only, while the inner regions still show some random motion. At the end of the simulation (Fig. 4.7), the initial rigid body rotation has smoothed out to a disk-like rotation. As in the unperturbed simulations, the system has become more compact which can be seen in Fig. 4.7 a).

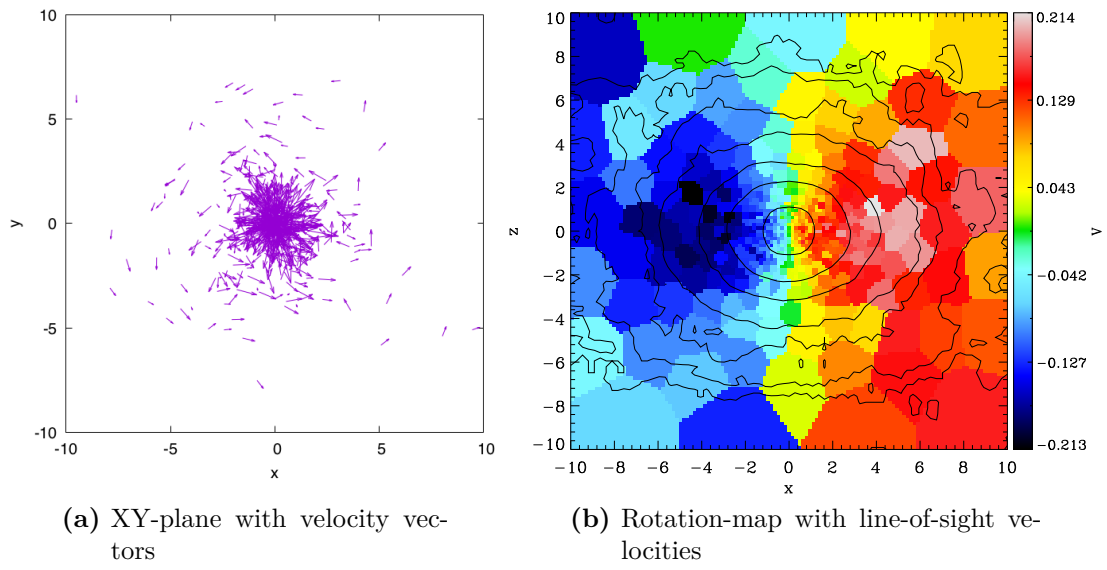


Figure 4.7.: Plot of rotational velocities at the end of the simulation

4.2. Central Mass

The second kind of perturbation discussed in this thesis is that of a compact central mass. Systems with either of the two density profiles used in these simulations can in principle house such a compact central mass. A system with a Hernquist profile, like an elliptical galaxy, most likely houses a supermassive black hole (SMBH). In a globular cluster with a Plummer profile, massive stars will eventually reach the end of their life and collapse to become neutron stars or stellar black holes. Through different effects, like collisions between compact objects or between compact objects and stars, as well as accretion of gas, these stellar black holes might grow. Due to dynamical friction the BHs will eventually settle down to the center of the cluster, like Kulkarni et al. (1993) propose. It is therefore justified to assume some kind of compact object at the center of these systems and therefore their impact in the evolution of ROI needs to be discussed. It has to be noted that both the development of SMBHs and the process of dynamical friction take a significant amount of time, so one has to assume the onset of ROI to be in a later stage of the lifetime of the system to resemble a real physical process. For an analytical approach to the problem of a central mass at the center of a system undergoing ROI see Palmer and Papaloizou (1988).

All simulations were run with the same timestep-size and the same softening length. Since the ellipticity of the systems is calculated within the half-mass radius, the central masses were excluded from the calculation of the HMR: As especially for the setups with $M_{\bullet} = 10^4 m$ the BHs contain a significant amount of mass of the entire cluster ($M_{\bullet} \approx 10^{-2} M_{tot}$). Including them in the calculation would shrink the HMR and therefore ruin the comparability between the different setups and the previous tests. By excluding them, only the stellar component is observed and compared to the unperturbed simulations.

4.2.1. Plummer Setup

As in the other chapters, analysis of the results begins with the Plummer setups. The parameters of the simulations can be found in Sec. III.2.2.

In contrast to the rotation setups, a central mass appears to have a much larger impact on the evolution of ellipticity (see Fig. 4.8). For dynamically warmer regimes until $\eta_{vir} = 0.16$ the influence of the central mass seems to be small and independent of M_{BH} . For $\log(\eta_{vir}) = 0.09$, $\log(M_{\bullet}) = 2$ and $\log(M_{\bullet}) = 4$ show almost the same ellipticity ϵ_2 , which would suggest that the impact of the effect is still independent of mass, but $\log(M_{\bullet}) = 3$ shows a much higher ellipticity ϵ_2 and appears almost perfectly prolate. The interesting implications of this will become more evident in Fig. 4.9 and will be discussed at that point. While for the lower mass BHs ($\log(M_{\bullet}) = 2 - 3$) and dynamically cold regimes ($\log(\eta_{vir}) = -4 - -2$) the effect seems to be negligible, it is very dominant for $\log(M_{\bullet}) = 4$: For these values of η_{vir} the central mass changes the shape drastically from a slight triaxiality in the unperturbed case to a very oblate shape.

Fig. 4.9 shows the interesting behaviour of the systems compared to the unperturbed

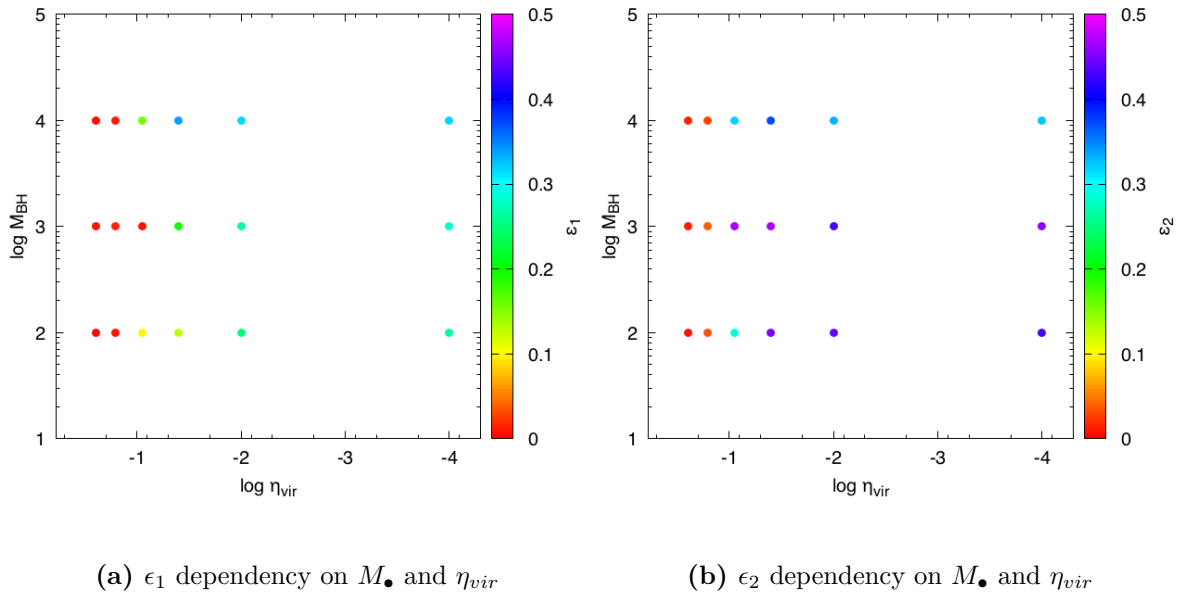


Figure 4.8.: Evolution of ellipticity under different conditions of black hole mass M_{BH} and virial ratio η_{vir}

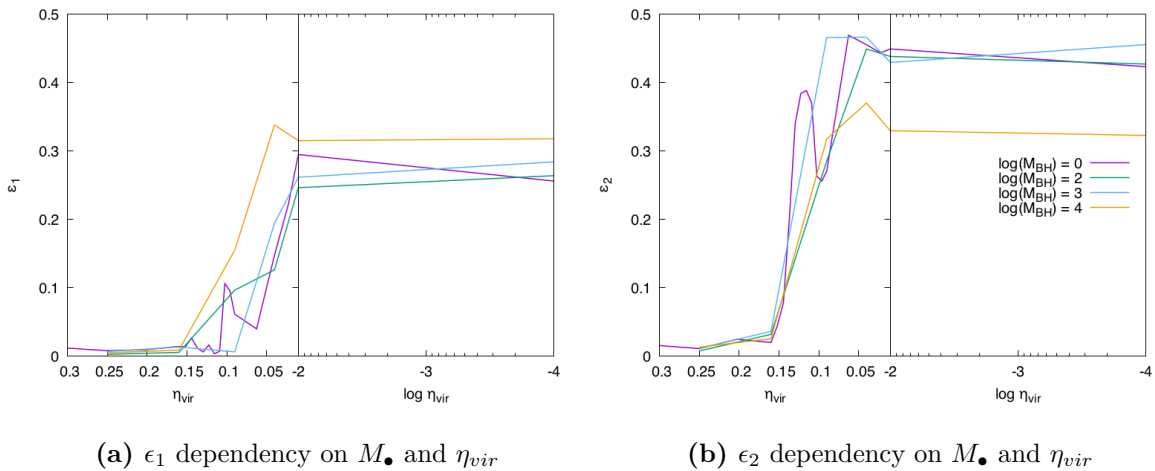


Figure 4.9.: Comparison of the influence on BH-mass to the ideal systems

case at three points. First at $\eta_{vir} = 0.09$: While $\log(M_\bullet) = 2$ is only slightly more triaxial than the unperturbed system, $\log(M_\bullet) = 3$ and $\log(M_\bullet) = 4$ differ a lot from the ideal case. Instead of the slightly triaxial shape of the unperturbed system, $\log(M_\bullet) = 3$ is almost perfectly prolate. It also does not follow the dip in ϵ_2 of the unperturbed case, which indicates that it suppresses the effect that causes ϵ_2 to decline in the ideal system. This would mean that a central mass of $\log(M_\bullet) = 3$ has a stabilising effect on the system

and helps it keep the final shape induced by ROI. To test this assumption it could be of interest to perform more simulations with varying central masses at values for η_{vir} that show a dip in ϵ_2 .

The system with $\log(M_\bullet) = 4$ also differs from the ideal system. The value for ϵ_1 is significantly higher than in the unperturbed system, which indicates a stronger triaxial shape of the resulting system.

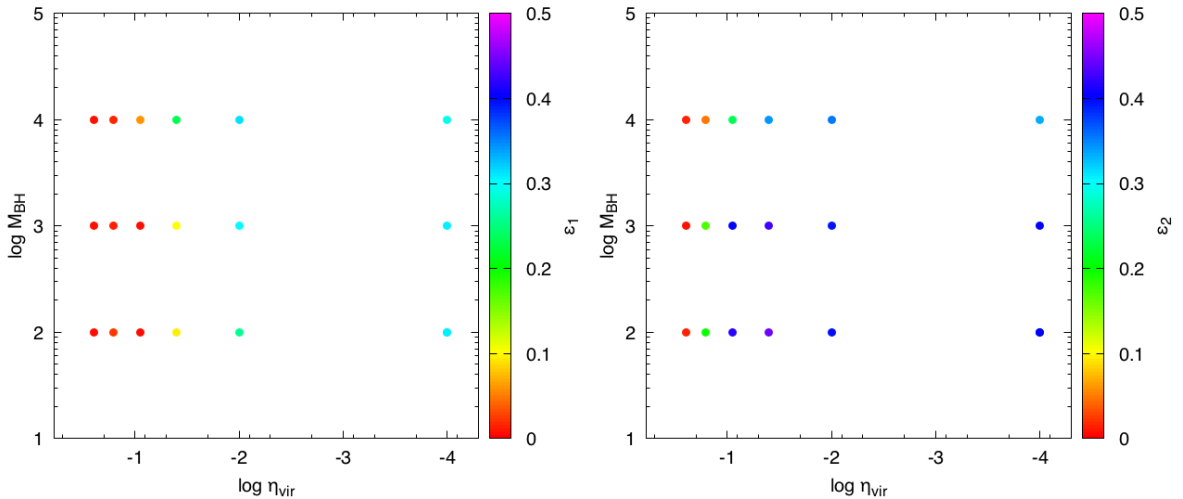
The next interesting point is at $\eta_{vir} = 0.04$: While $\log(M_\bullet) = 2 - 3$ fit the unperturbed case very well, except for a more triaxial shape in the $\log(M_\bullet) = 3$ system, the values of $\epsilon_{1,2}$ for $\log(M_\bullet) = 4$ differ significantly from the ideal system. ϵ_1 is a lot higher than in the unperturbed case, while ϵ_2 is a lot lower, giving the system a very oblate shape with a slight tendency towards triaxiality.

The third point of interest is at $\log(\eta_{vir}) = -2$: $\log(M_\bullet) = 2 - 3$ have grown in triaxiality, with $\log(M_\bullet) = 3$ being slightly more triaxial. The setup with $\log(M_\bullet) = 4$ has decreased in both ellipticities $\epsilon_{1,2}$, while still staying oblate.

While there is strong evidence for an impact of a central mass on ROI in a Plummer sphere, there seems to be no obvious correlation between mass and suppression of ellipticity.

4.2.2. Hernquist Setup

In contrast to the Plummer setups, the simulations with $\log(M_\bullet) = 2 - 3$ appear to have less of an effect on the final ellipticity. Only the value of ϵ_1 is higher for the $\log(M_\bullet) = 3$ system which hints towards a stronger triaxiality. The impact of a central mass on the



(a) ϵ_1 dependency on M_\bullet and η_{vir}

(b) ϵ_2 dependency on M_\bullet and η_{vir}

Figure 4.10.: Evolution of ellipticity under different conditions of black hole mass M_{BH} and virial ratio η_{vir}

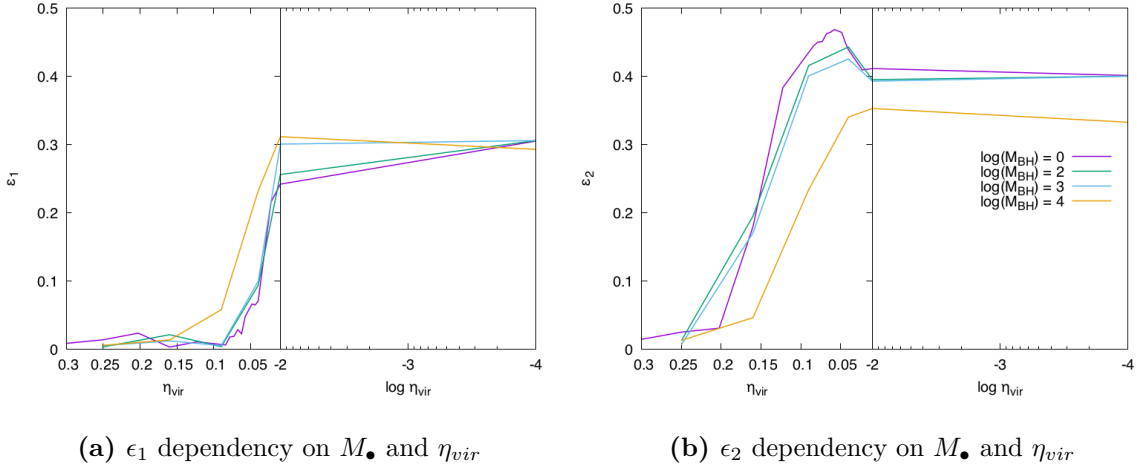


Figure 4.11.: Comparison of the influence on BH-mass to the ideal systems

evolution of ellipticity becomes apparent for the $\log(M_\bullet) = 4$ setups. A clear suppression of the ϵ_2 ellipticity can be observed starting from $\eta_{vir} = 0.16$.

To better portray this behaviour the ellipticities are plotted against the ideal case in Fig. 4.11. At $\eta_{vir} = 0.16$ the value for ϵ_2 in the $\log(M_\bullet) = 4$ system is significantly lower than in the ideal case, while ϵ_1 is slightly higher. This means that the system is still fairly spherically symmetric at this point, with a slight tendency towards oblateness. These two observations indicate that the onset of ROI in the $\log(M_\bullet) = 4$ system is suppressed and significantly shifted towards dynamically colder regimes.

As η_{vir} decreases, the systems with $\log(M_\bullet) = 2 - 3$ stay quite close to their unperturbed counterpart. Even though the effect appears small it has to be noted that the $\log(M_\bullet) = 3$ ellipticity ϵ_2 always stays below the ones for $\log(M_\bullet) = 2$ and the ideal case. These values are too small to decide whether the effect is really of suppressing nature, but it would indicate that the threshold for the beginning impact of a central mass on the evolution of ROI is somewhere of the order of magnitude $M_\bullet = 10^3$. It would be of interest to conduct more tests with varying M_\bullet to further pinpoint that threshold, but this surpasses the capacity of this thesis.

At $\log(\eta_{vir}) = -2$ both values of ϵ_1 in the $\log(M_\bullet) = 2$ and $\log(M_\bullet) = 3$ systems are lower than the unperturbed value, which indicates a more triaxial shape of the final system. Together with the fact that the value of ϵ_1 at $\log(\eta_{vir}) = -4$ only slightly differs from that at $\log(\eta_{vir}) = -2$ in the $\log(M_\bullet) = 2$ system and stays the same in the $\log(M_\bullet) = 3$ system, this indicates that the systems reach their final triaxiality, as observed in the other tests, at larger values of η_{vir} .

The system with $\log(M_\bullet) = 4$ shows the most promising results for the impact of a central mass on ROI evolution. Especially the ϵ_2 values appear to be damped by M_{BH} , as the difference in ellipticity between the unperturbed system and that with $\log(M_\bullet) = 4$ stays fairly constant at $\Delta\epsilon_1 \approx 0.1 - 0.2$. It would be interesting to check for a correlation between the mass of the central object and this dampening of ellipticity, but that would

require more simulations with different M_\bullet and is therefore best suited for future work. The values of ϵ_1 also appear to be influenced in a way that indicates a changed evolution of the final shape after the ROI set in. While for the undisturbed systems the resulting shape is predominantly prolate, the systems with a central mass become more triaxial and oblate as the central mass increases and η_{vir} decreases.

For a detailed look on the evolution of ROI in the systems with $\log(M_\bullet) = 4$, Fig. 4.12 through Fig. 4.14 show the evolution of ellipticity over the time of the simulation in the system with central mass, compared to the system without central mass.

In the $\eta_{vir} = 0.16$ system (Fig. 4.12) with central mass the suppression of the onset of ROI is very evident. There is a slight increase in ellipticity ϵ_2 in the same period of the simulation, as in the system without a central mass, but the maximum value of ϵ_2 is a lot lower for the case with the BH. In both cases, both ϵ_1 and ϵ_2 stay fairly constant in the time after they have reached their respective maximum values.

In the $\eta_{vir} = 0.09$ setup (fig. 4.13) the effect of suppression is just as dominant. While the maximum ellipticity ϵ_2 is only slightly lower in the system with central mass than in the system without, the value of ϵ_2 decreases right after the maximum, whereas the value stays fairly constant in the unperturbed system.

Fig. 4.14 shows the system with $\eta_{vir} = 0.04$. Here the effect of the BH on ϵ_1 becomes very apparent. While the other perturbed simulations ended in prolate shapes, like the unperturbed ones, the central mass seems to increase the triaxiality of the resulting system until it becomes almost oblate, as discussed earlier in this section.

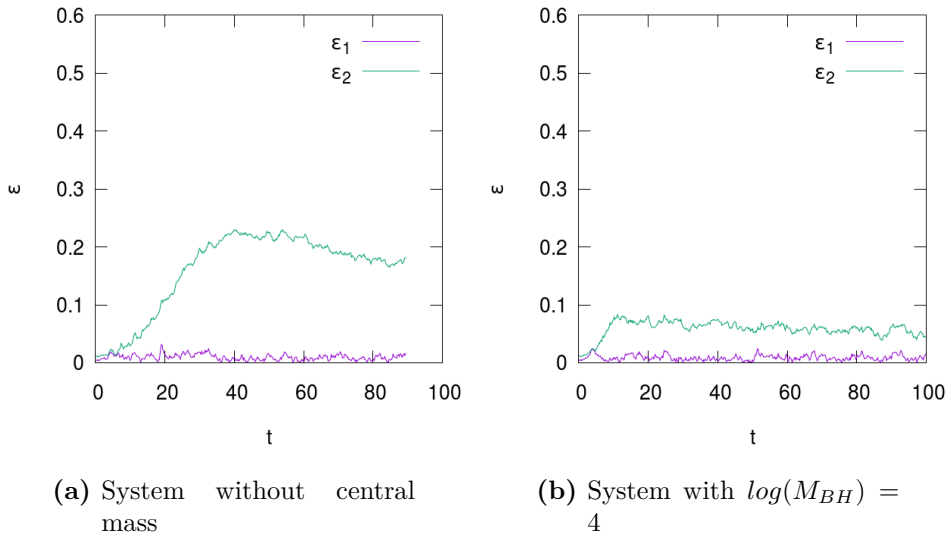


Figure 4.12.: Suppressing effect of the central mass in the systems with $\eta_{vir,0} = 0.16$

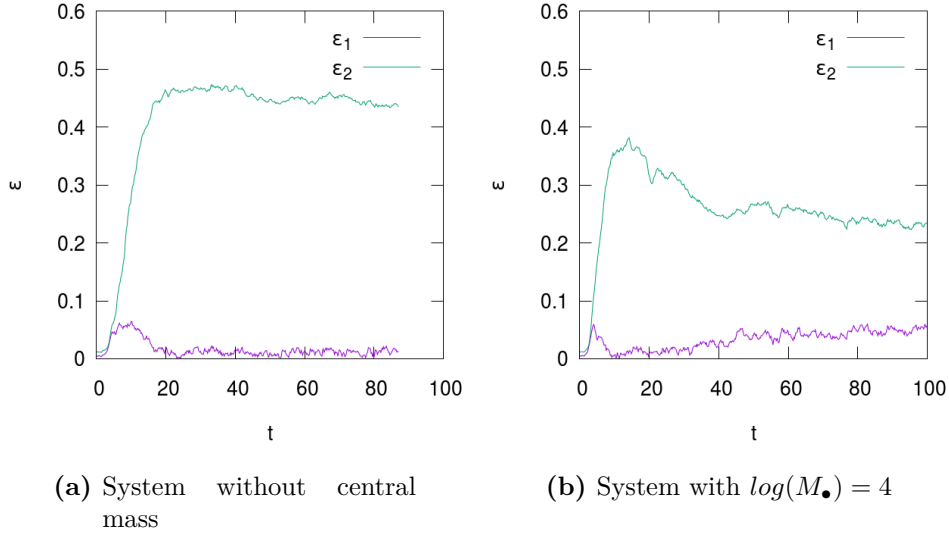


Figure 4.13.: Suppressing effect of the central mass in the systems with $\eta_{vir} = 0.09$

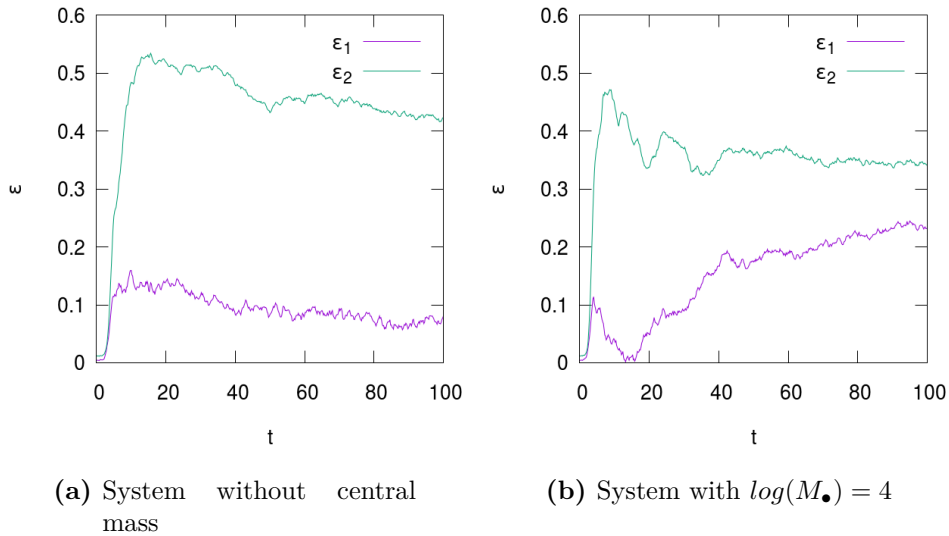


Figure 4.14.: Suppressing effect of the central mass in the systems with $\eta_{vir} = 0.04$

5. Summary and Conclusion

In this work the evolution of Radial Orbit Instability was studied for setups of Plummer- & Hernquist spheres, with the goal to understand the evolution and resulting intrinsic ellipticities ϵ under different virial coefficients η_{vir} . Additional to these ideal setups, the influence of an added rotation and a central mass on these results was studied.

Undisturbed ROI

Chapter 3 gave an overview of the properties of ROI in unperturbed systems. The evolution of the intrinsic ellipticities ($\epsilon_{1,2}$) was evaluated and most systems showed a violent increase in ϵ_2 , which lead to a prolate shape that indicates the onset of Radial Orbit Instability. From the resulting final ellipticities of the systems, thresholds of η_{vir} for the onset of ROI in the Plummer and Hernquist systems were found. These appear to be at $\eta_{vir} \approx 0.16$ for the Plummer systems and $\eta_{vir} \approx 0.2$ for the Hernquist systems. Both spheres show a maximum in ϵ_2 at $\eta_{vir} = 6.25 \cdot 10^{-2}$ and remain fairly prolate until that point. After the maximum the systems became more and more triaxial, until they reached a constant value for ϵ_1 and ϵ_2 at $\log(\eta_{vir}) = -4$, which they kept until the system with the smallest initial virial ratio of $\log(\eta_{vir}) = -16$. Only a dip in ϵ_2 accompanied by an increase in ϵ_1 in the Plummer systems at $\eta_{vir} = 0.09$ disturbed this evolution and caused a discussion of resolution.

Tests with a smaller timestep size and softening length indicated that the resulting ellipticities vary slightly with these properties. A higher resolution caused the Plummer systems to undergo a second change in shape, from a predominantly prolate configuration, to a triaxial one. This change also happens for lower resolution simulations around $\eta_{vir} = 0.09$. It takes place in the last 10% – 20% of the simulation time for the lower resolution simulations and is shifted forward in time with higher resolution and decreasing virial coefficient η_{vir} . This indicates that the onset of rising triaxiality is shifted towards larger values of η_{vir} in simulations with smaller timestep sizes and smaller softening length. As to why this change in shape happens also for distinct lower resolution simulations is not yet clear and should be studied in more detail. Likewise more high-resolution tests should be conducted, to see if the onset of ROI is shifted as well, or if even high-resolution simulations only undergo this second change of shape after a critical value for η_{vir} . The only available data for a high-resolution test in the dynamically warmer regime could indicate a second change in shape, as the decrease of ϵ_2 had already begun, but this data is not sufficient to find a conclusion.

The Hernquist systems showed no second change in shape at higher resolutions, but kept their maximum values for ϵ_1 and ϵ_2 over the entire time of the simulation. Only the onset

of ROI was shifted to smaller values of η_{vir} .

Disturbed ROI

To test the impact of perturbations on the evolution of the shape of systems that have undergone ROI, numerous tests with rotation and a compact central mass were conducted.

For the rotation no significant impact on either of the spheres was found. Only for the additional tests with exceedingly large rotational velocities in the Hernquist profile, a slight indication for an increase in ellipticity in the dynamically warmer regimes was found. The way the rotation was set up as a rigid body rotation, whereas neither elliptical galaxies, nor globular clusters show a rigid body rotation around an axis, and the high rotational velocities needed to find a difference in the evolution, make it unlikely that a setup like this can resemble a real physical system.

This in turn is a soothing result for other systems that might undergo ROI, as rotation is a widely found feature in different stellar systems and rotation around an axis seems to play no significant role in the evolution of ROI.

The simulations with a compact central mass showed more promising results.

In the Plummer setups the systems with $\log(M_{\bullet}) = 3$ seemed to suppress the destabilisation that caused the ellipticity ϵ_2 to decline around $\eta_{vir} = 0.09$ and caused the system to become more triaxial at that point than the ideal system without a central mass. Besides the suppression of the decline in ϵ_2 , the systems for $\log(M_{\bullet}) = 3$ stayed fairly close to the unperturbed case and $\log(M_{\bullet}) = 2$ showed barely any deviation. The setups with the most massive central masses with $\log(M_{\bullet}) = 4$ differed most from the unperturbed results. While the dynamically warm setups showed no difference to the unperturbed ones, the systems that underwent ROI showed none of the expected prolate shapes typical for ROI, but instead started out as triaxial and then became oblate.

For the Hernquist systems the effect was essentially the same. With increasing mass of the central object the values for ϵ_2 were decreased. While ϵ_2 decreased, ϵ_1 increased, which caused the system to become more triaxial. Another result was that the decrease of ϵ_2 seems to scale with the central mass in the Hernquist systems. While $\log(M_{\bullet}) = 3$ only slightly decreased the resulting ϵ_2 , the impact of $\log(M_{\bullet}) = 4$ was significant. This leads to the assumption that the beginning of the effect of a central mass on ROI lies between $\log(M_{\bullet}) = 3$ and $\log(M_{\bullet}) = 4$. In addition to that, the onset of ROI appeared to be shifted to dynamically colder initial conditions for $\log(M_{\bullet}) = 4$. This means that a sufficiently large central mass seems to suppress the ROI until a certain value of η_{vir} . To get the exact relation between M_{\bullet} and η_{vir} required for this suppression, more tests will have to be conducted.

However, the required mass needed to have an effect on ROI imposes a problem on the applicability to real physical systems. In the conducted tests, a mass of $\log(M_{BH}) = 3$ means that $M_{BH} \approx 10^{-2} M_{tot}$. For a globular cluster with $M_{tot} \approx 10^6 M_{\odot}$ this would

lead to $M_{BH} \approx 10^4 M_{\odot}$. Black holes in GCs are believed to be of stellar origin, which would give them masses of $M_{\bullet} \approx 3 - 10 M_{\odot}$. Even taken into account that recent measurements of gravitational waves from the LIGO observatory are believed to originate in GCs and that these measurements indicate black hole mergers between black holes of $M_{\bullet} \approx 20 - 30 M_{\odot}$, the resulting BHs are more than two orders of magnitude smaller than the required masses.

For elliptical galaxies like Messier 87, with a total mass of $M_{tot} \approx 10^{12} M_{\odot}$ the BH-mass would be $M_{\bullet} \approx 10^{10} M_{\odot}$. While elliptical galaxies seem to host the most massive SMBHs known to this date and can reach masses of $M_{\bullet} > 10^{10} M_{\odot}$ (see for example Hlavacek-Larrondo et al. (2013)), one has to take into account the accretion timescales for them to reach these masses. To account for that, the ROI would have to happen at a very late stage in the dynamic evolution of the stellar system. This is in contrast to the suggestion by Burkert (1990) who discusses ROI as a reason for the shape of elliptical galaxies. In this concept the galaxies undergo a short, initial starburst-phase after which they experience a violent collapse.

In order to address this problem, it would be of interest to study the impact of particle-number and timestep-size of the simulation on the mass-dependency of the effect on the resulting geometric shape. If a higher particle-resolution could reduce the required mass for an evident impact on the resulting shape, this could indicate a more realistic result.

Radial Orbit Instability in Cold Dark Matter Halos

The suppression of ROI in systems with a central mass could also be relevant for simulations of the impact of ROI on cold dark matter halos (CDMHs) (for example carried out by MacMillan et al. (2006)). With the galaxy inside a CDMH being only a small fraction of the size of the halo, it can be viewed as a relatively compact central mass. If the CDMH is then disturbed, for example by interaction with other halos in a galaxy cluster, as Frank C. van den Bosch (2017) suggests, and a Radial Orbit Instability is induced, the gas component might not be negligible. This would indicate that the observation of isolated CDMHs, as done by MacMillan et al. (2006), is not sufficient to accurately describe the resulting geometric configuration of such systems. This is supported by the results of Ceverino et al. (2015) who find that if the baryonic mass of galaxies within a DMH is large enough, the resulting galaxy will become more oblate, instead of prolate as induced by the DMH.

The suppression of ellipticity seems to have no effect on the resulting density profile, however, as Fig. III.10 indicates and therefore does not affect the elegant theory of MacMillan et al. (2006) to explain the shape of the NFW-profile. Nevertheless it would be of interest to further study the impact of central masses on the evolution of shape in the Radial Orbit Instability. Either with the beforementioned upscaling of particle numbers and higher timestep resolution, or with a galaxy at the center of a dark matter halo, as Ceverino et al. (2015) do.

Bibliography

Antonov, V. A.

1961. Remarks on the problem of stability in stellar dynamics. *Soviet Astronomy, Vol. 4, p.859*, 4:859.

Barnes, J. and P. Hut

1986. A hierarchical $O(n \log n)$ force-calculation algorithm. *Nature*, 324(6096):446–449.

Bellovary, J. M., J. J. Dalcanton, A. Babul, T. R. Quinn, R. W. Maas, C. G. Austin, L. L. R. Williams, and E. I. Barnes

2008. The role of the radial orbit instability in dark matter halo formation and structure. *The Astrophysical Journal*, 685(2):739–751.

Binney, J. and S. Tremaine

2011. *Galactic Dynamics: (Second Edition) (Princeton Series in Astrophysics)*. Princeton University Press.

Burkert, A.

1990. The dissipationless evolution of elliptical galaxies. *Monthly Notices of the Royal Astronomical Society*, 247:152.

Ceverino, D., J. Primack, and A. Dekel

2015. Formation of elongated galaxies with low masses at high redshift. *Monthly Notices of the Royal Astronomical Society*, 453(1):408–413.

Chomiuk, L., J. Strader, T. J. Maccarone, J. C. A. Miller-Jones, C. Heinke, E. Noyola, A. C. Seth, and S. Ransom

2013. A radio-selected black hole x-ray binary candidate in the milky way globular cluster m62. *The Astrophysical Journal*, 777(1):69.

Frank C. van den Bosch, Go Ogiya, O. H. A. B.

2017. Disruption of dark matter substructure: Fact or fiction?

Henon, M.

1973. Numerical experiments on the stability of spherical stellar systems. *Astronomy and Astrophysics*, Vol. 24:p. 229.

Hernquist, L.

1987. Performance characteristics of tree codes. *The Astrophysical Journal Supplement Series*, 64:715.

- Hernquist, L.
1990. An analytical model for spherical galaxies and bulges. *The Astrophysical Journal*, 356:359.
- Hlavacek-Larrondo, J., S. W. Allen, G. B. Taylor, A. C. Fabian, R. E. A. Canning, N. Werner, J. S. Sanders, C. K. Grimes, S. Ehlert, and A. von der Linden
2013. Probing the extreme realm of agn feedback in the massive galaxy cluster, rx j1532.9+3021. *The Astrophysical Journal*.
- Kulkarni, S. R., P. Hut, and S. J. McMillan
1993. Stellar black holes in globular clusters. *Nature*, 364(6436):421–423.
- Lynden-Bell, D.
1967. Statistical mechanics of violent relaxation in stellar systems. *Monthly Notices of the Royal Astronomical Society*, 136(1):101–121.
- Maccarone, T. J., A. Kundu, S. E. Zepf, and K. L. Rhode
2007. A black hole in a globular cluster. *Nature*, 445(7124):183–185.
- MacMillan, J. D., L. M. Widrow, and R. N. Henriksen
2006. On universal halos and the radial orbit instability. *The Astrophysical Journal*, 653(1):43–52.
- Maréchal, L. and J. Perez
2011. Radial orbit instability: review and perspectives. *Transport Theory and Statistical Physics*, 40(6-7):425–439.
- Merritt, D. and L. A. Aguilar
1985. A numerical study of the stability of spherical galaxies. *Monthly Notices of the Royal Astronomical Society*, 217:787–804.
- Navarro, J. F., C. S. Frenk, and S. D. M. White
1996. The structure of cold dark matter halos. *Astrophysical Journal v.462*, p.563.
- Obreja, A., G. S. Stinson, A. A. Dutton, A. V. Macciò, L. Wang, and X. Kang
2016. Nihao vi. the hidden discs of simulated galaxies. *Monthly Notices of the Royal Astronomical Society*, 459(1):467–486.
- Palmer, P. L. and J. Papaloizou
1987. Instability in spherical stellar systems. *Monthly Notices of the Royal Astronomical Society*, 224:1043–1053.
- Palmer, P. L. and J. Papaloizou
1988. The stability of spherical stellar systems with a compact central mass. *Monthly Notices of the Royal Astronomical Society*, 231:935–951.

- Plummer, H. C.
1911. On the problem of distribution in globular star clusters. *Monthly Notices of the Royal Astronomical Society*, 71:460–470.
- Polyachenko, E. V., V. L. Polyachenko, and I. G. Shukhman
2011. Notes on the stability threshold for radially anisotropic polytrope. *Monthly Notices of the Royal Astronomical Society*, 416(3):1836–1843.
- Polyachenko, E. V. and I. G. Shukhman
2015. On the nature of the radial orbit instability in spherically symmetric collisionless stellar systems. 41:1–13.
- Polyachenko, E. V. and I. G. Shukhman
2016. On one classical problem in the radial orbit instability theory. *Astronomy Letters*, 42(2):100–114.
- Polyachenko, E. V. and I. G. Shukhman
2017. Radial orbit instability in systems of highly eccentric orbits: Antonov problem reviewed. *Monthly Notices of the Royal Astronomical Society*, 470(2):2190–2203.
- Polyachenko, V. L.
1991. Theory of the radial-orbit instability as a universal cause of structure formation in stellar systems. *Soviet Journal of Experimental and Theoretical Physics Letters*, 54:555–558.
- Polyachenko, V. L.
1992a. Radial orbit instability as a mechanism of formation of elliptical galaxies. *Soviet Journal of Experimental and Theoretical Physics*, 36:482.
- Polyachenko, V. L.
1992b. Theory and applications of radial orbit instability in collisionless gravitational systems. *Soviet Journal of Experimental and Theoretical Physics*, 74:755–763.
- Polyachenko, V. L. and I. G. Shukhman
1981. General models of collisionless spherically symmetric stellar systems - a stability analysis. *Soviet Journal of Experimental and Theoretical Physics Letters*, 25:533.
- Theis, C. and R. Spurzem
1998. On the evolution of shape in n-body simulations. *Astronomy & Astrophysics*.
- Trenti, M. and G. Bertin
2006. Partial suppression of the radial orbit instability in stellar systems. *The Astrophysical Journal*, 637:717–726.
- van Albada, T. S.
1982. Dissipationless galaxy formation and the r to the $1/4$ -power law. *Monthly Notices of the Royal Astronomical Society*, 201:939–955.

List of Figures

1.1.	"Tuning-Fork" Diagram: Display of the two different possible developments of the instability, as presented by Polyachenko (1992b)	2
1.2.	Ideal plots of the density profiles	4
2.1.	Concept of a Treecode. Image Credit: Nyland et al (1993)	7
2.2.	Code Properties: Order of processing time (left) and impact of timestep size on a leapfrog integrator (right)	8
2.3.	The vectors indicate the direction and magnitude of the added rotational velocity. Plotted are only a small fraction of the particles. The signs in the transformation lead to a counter-clockwise rotation around the z-axis.	14
2.4.	Stability of the Plummer-Profile against change in the softening-length ϵ	16
2.5.	Stability of the Hernquist-Profile against change in the softening-length ϵ	16
2.6.	A direct comparison between the development of the total energy in the high-resolution and low-resolution simulation "P-HighRes-0,25" and "P-0,25" (see Sec. III.2.1 for Parameters).	17
2.7.	Kinetic-, potential and total energy are plottet over the entire simulation-time. The green and purple line in the center correspond to the lines for high- and low resolution in Fig. 2.6 with the same colors. The red lines resemble kinetic energy, while the blue lines resemble potential energy. Solid and dashed lines correspond to high- and low resolution, respectively.	18
3.1.	Plummer-profile: Initial condition	24
3.2.	Plummer-profile: At the First infall	24
3.3.	Plummer-profile: After the turnaround point	25
3.4.	Plummer-profile: Density-waves form	25
3.5.	Plummer-profile: The density waves move outwards	26
3.6.	Plummer-profile: The beginning of phase-mixing	26
3.7.	Plummer-profile: The inner shells appear phase-mixed	27
3.8.	Plummer-profile: End of the simulation	28
3.9.	Evolution of HMR, ellipticity and η_{vir}	28
3.10.	Evolution of ellipticity with decreasing η_{vir}	30
3.11.	Evolution of ϵ and η_{vir} in the system "P-0,31"	31
3.12.	Evolution of ellipticity with decreasing η_{vir}	32
3.13.	Evolution of HMR, ellipticity and η_{vir} in the Hernquist system "H-e-4", see Sec. III.2.1 for parameters.	33
3.14.	Resolution-impact on Plummer-profile	34

3.15. Evolution of ellipticities. Solid lines: high-resolution simulations. Dashed lines: low-resolution simulations.	35
3.16. Resolution-impact on Hernquist-profile	36
3.17. Evolution of ellipticities. Solid lines: high-resolution simulations. Dashed lines: low-resolution simulations.	37
4.1. Evolution of the ellipticity under different conditions of rotational velocity Ω and virial coefficient η_{vir} . Both Ω and η_{vir} are displayed logarithmically, while the values of ϵ are color-coded.	40
4.2. Comparison of the ellipticities to those of the systems without rotation. . .	41
4.3. Evolution of ellipticity in the systems with $\eta_{vir} = 0.09$. Solid lines: System with rotation. Dashed lines: System without rotation.	41
4.4. Evolution of ellipticity under different conditions of rotational velocity Ω and virial coefficient η_{vir}	42
4.5. Evolution of ellipticity under different conditions of rotational velocity Ω and virial coefficient η_{vir}	43
4.6. Plot of rotational velocities in the initial conditions	43
4.7. Plot of rotational velocities at the end of the simulation	44
4.8. Evolution of ellipticity under different conditions of black hole mass M_{BH} and virial ratio η_{vir}	46
4.9. Comparison of the influence on BH-mass to the ideal systems	46
4.10. Evolution of ellipticity under different conditions of black hole mass M_{BH} and virial ratio η_{vir}	47
4.11. Comparison of the influence on BH-mass to the ideal systems	48
4.12. Suppressing effect of the central mass in the systems with $\eta_{vir,0} = 0.16$. . .	49
4.13. Suppressing effect of the central mass in the systems with $\eta_{vir} = 0.09$. . .	50
4.14. Suppressing effect of the central mass in the systems with $\eta_{vir} = 0.04$. . .	50
III.1. Hernquist-profile: Initial condition	61
III.2. Hernquist-profile: First infall	61
III.3. Hernquist-profile: After the turnaround point	62
III.4. Hernquist-profile: Formation of density-waves	62
III.5. Hernquist-profile: Shells move outwards	63
III.6. Hernquist-profile: Beginning of phase-mixing	63
III.7. Hernquist-profile: Inner shells appear phase-mixed	64
III.8. Hernquist-profile: End of the simulation	64
III.9. Evolution of hmr and ellipticity during the time of the simulation	65
III.10. Comparison of initial and final density with central mass and in the ideal case	65

III. Appendix

III.1. Additional Plots

III.1.1. Dynamical Evolution of the Hernquist Profile

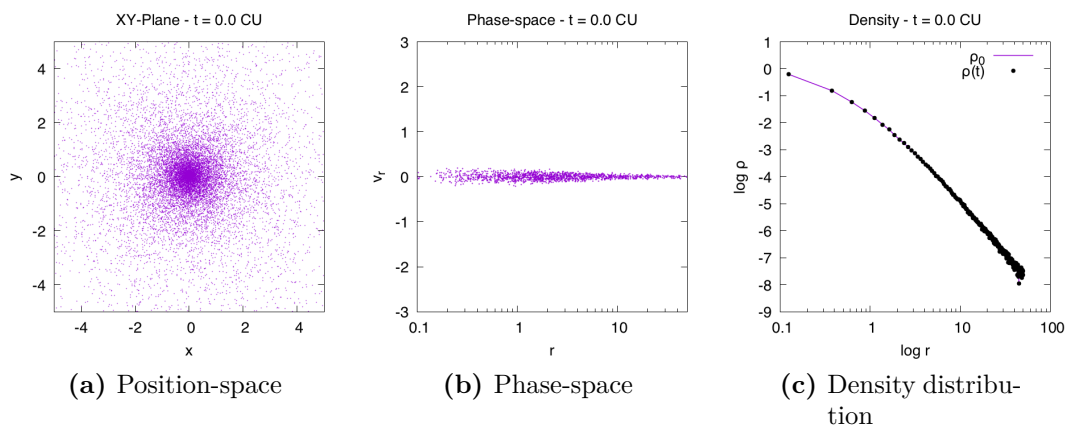


Figure III.1.: Hernquist-profile: Initial condition

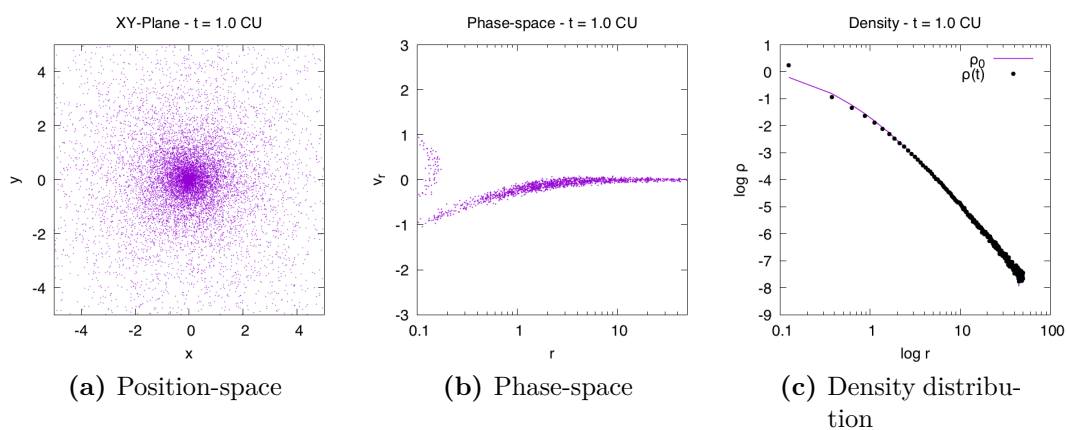


Figure III.2.: Hernquist-profile: First infall

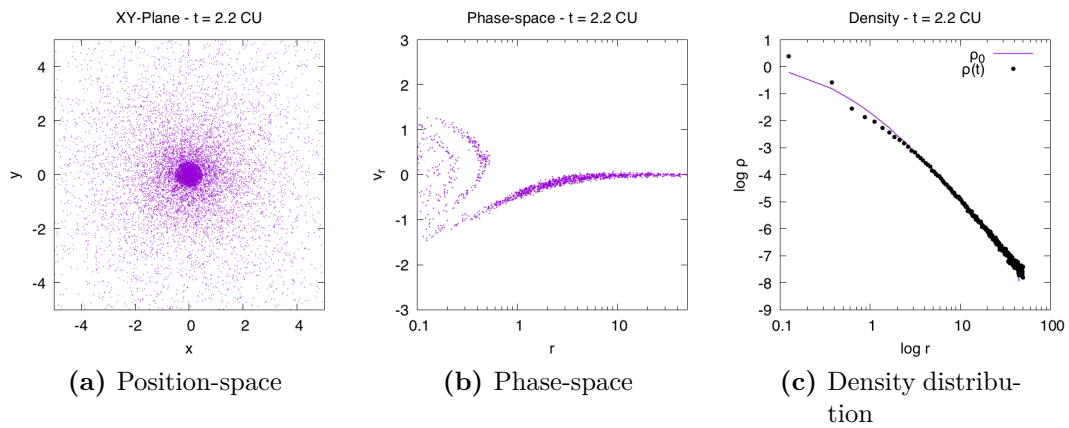


Figure III.3.: Hernquist-profile: After the turnaround point

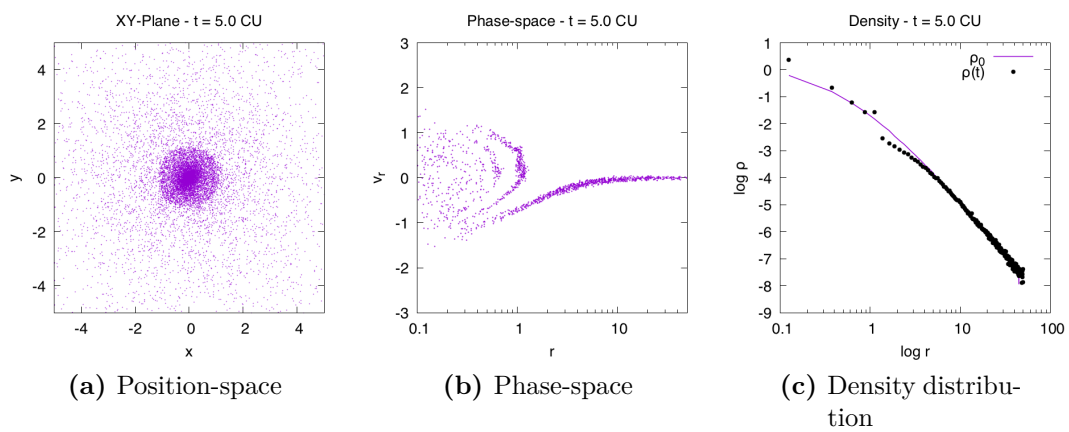


Figure III.4.: Hernquist-profile: Formation of density-waves

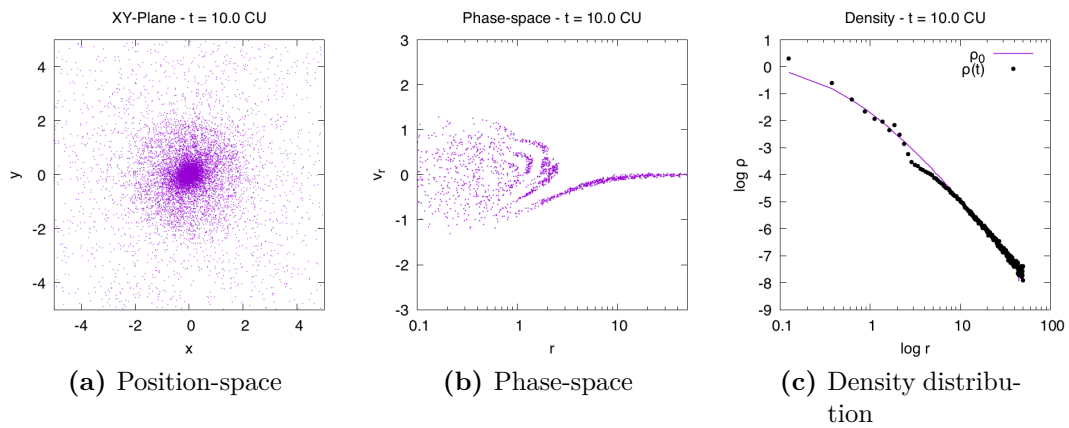


Figure III.5.: Hernquist-profile: Shells move outwards

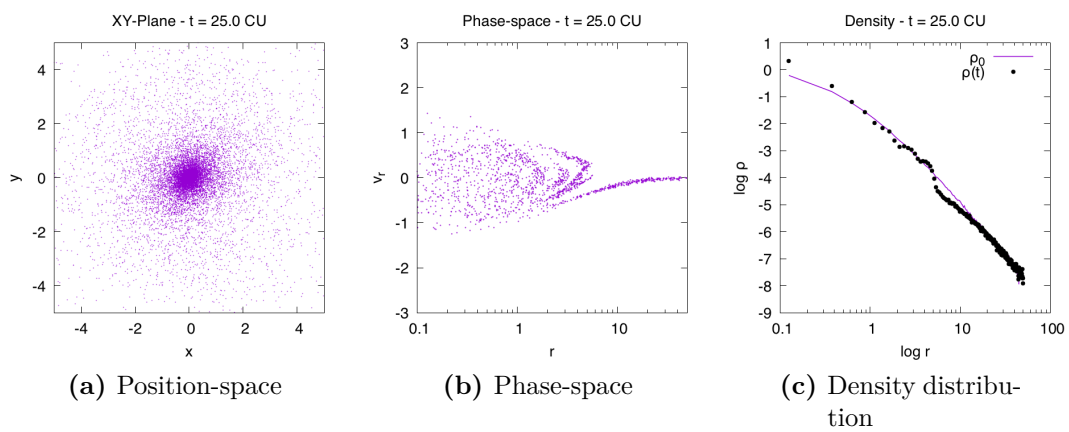


Figure III.6.: Hernquist-profile: Beginning of phase-mixing

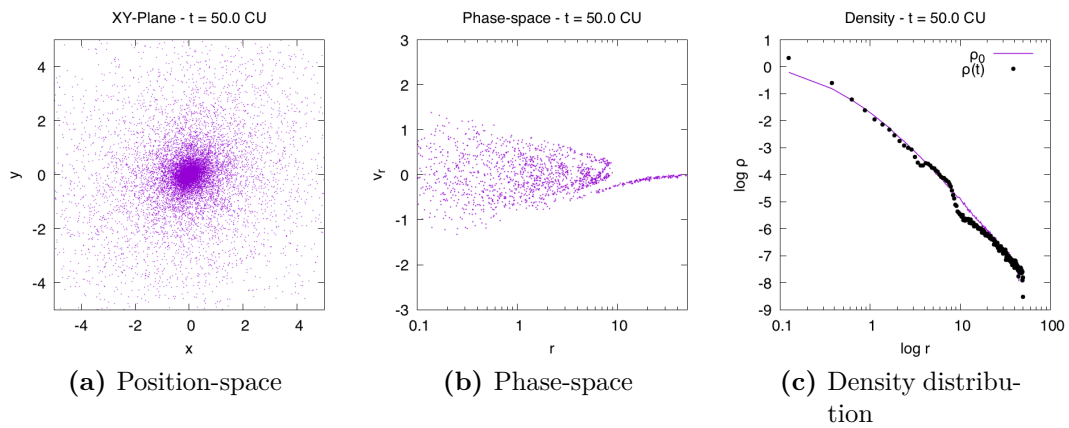


Figure III.7.: Hernquist-profile: Inner shells appear phase-mixed

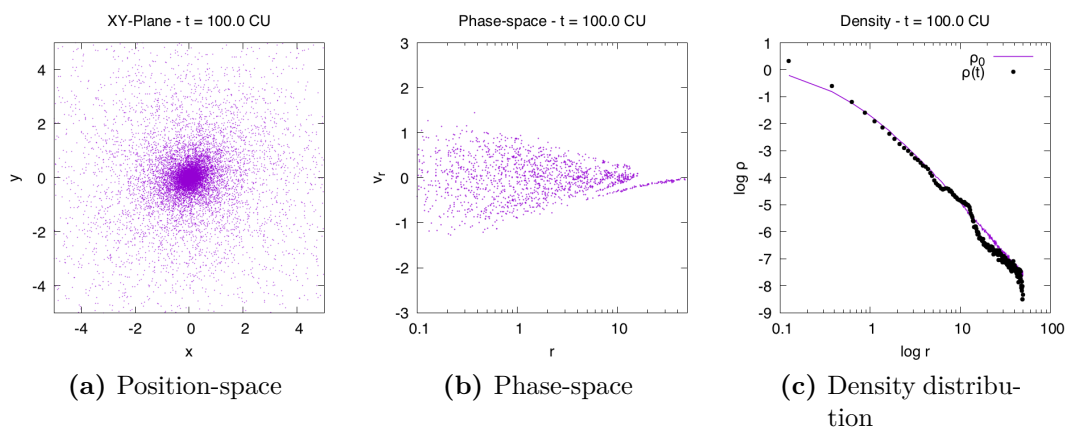


Figure III.8.: Hernquist-profile: End of the simulation

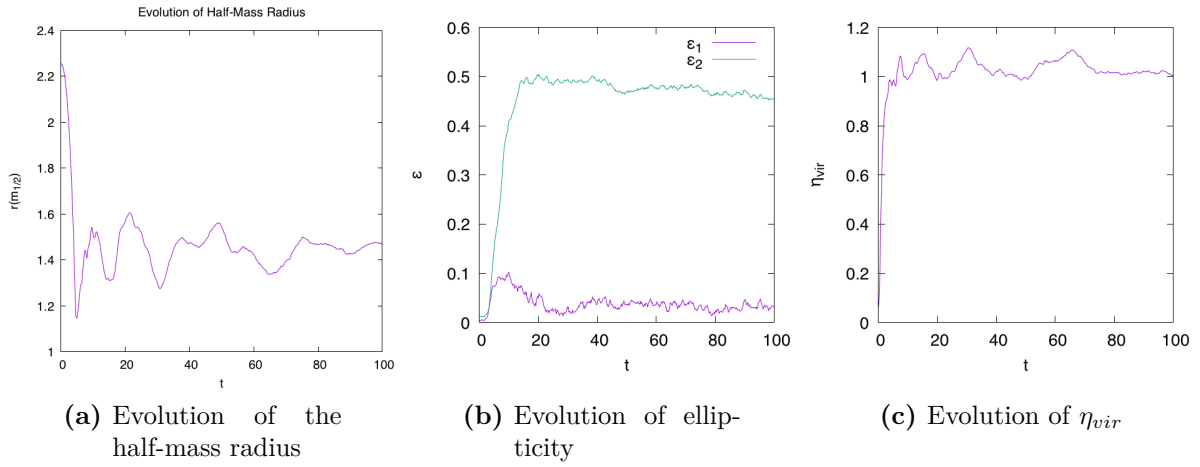


Figure III.9.: Evolution of hmr and ellipticity during the time of the simulation

III.1.2. Effect of central mass on the Hernquist profile

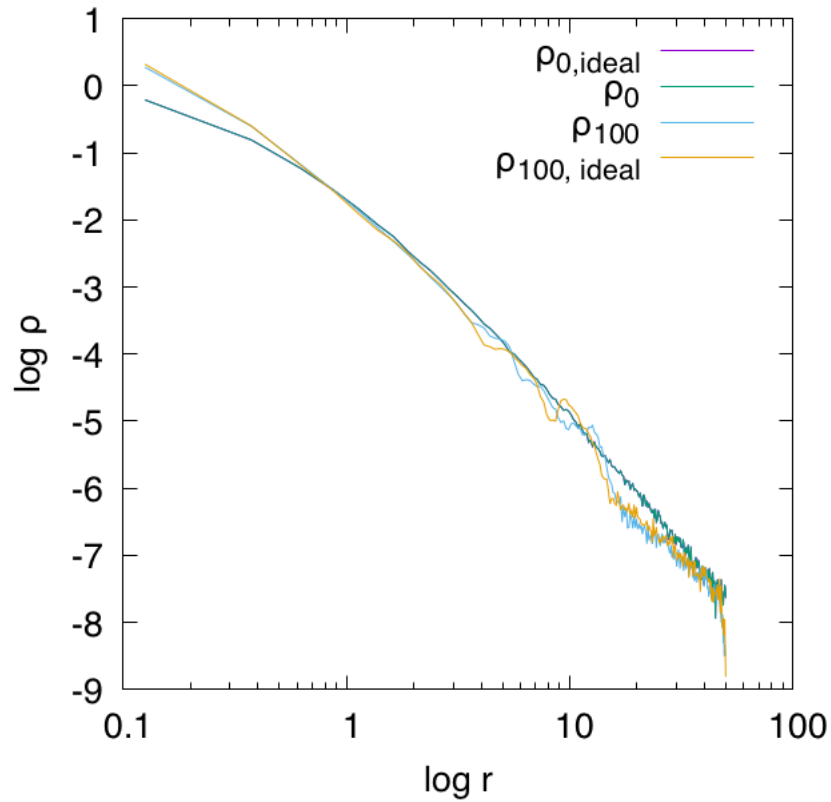


Figure III.10.: Comparison of initial and final density with central mass and in the ideal case

III.2. List of Simulations

III.2.1. Undisturbed ROI

Plummer

Name of the Simulation	χ	η_{vir}	run-time	Δ snap	Δt	ϵ
P-1,0	1,0	1,0	100	0,2	0,01	0,05
P-0,95	0,95	$9,025 \cdot 10^{-1}$	100	0,2	0,005	0,05
P-0,90	0,9	$8,1 \cdot 10^{-1}$	100	0,2	0,01	0,05
P-0,85	0,85	$7,225 \cdot 10^{-1}$	100	0,2	0,005	0,05
P-0,80	0,8	$6,4 \cdot 10^{-1}$	100	0,2	0,01	0,05
P-0,75	0,75	$5,625 \cdot 10^{-1}$	100	0,2	0,005	0,05
P-0,70	0,7	$4,9 \cdot 10^{-1}$	100	0,2	0,01	0,05
P-0,65	0,65	$4,225 \cdot 10^{-1}$	100	0,2	0,005	0,05
P-0,60	0,6	$3,6 \cdot 10^{-1}$	100	0,2	0,01	0,05
P-0,55	0,55	$3,025 \cdot 10^{-1}$	100	0,2	0,005	0,05
P-0,50	0,5	$2,5 \cdot 10^{-1}$	100	0,2	0,01	0,05
P-0,45	0,45	$2,025 \cdot 10^{-1}$	100	0,2	0,005	0,05
P-0,40	0,4	$1,6 \cdot 10^{-1}$	100	0,2	0,01	0,05
P-0,39	0,39	$1,521 \cdot 10^{-1}$	100	0,2	0,01	0,05
P-0,38	0,38	$1,444 \cdot 10^{-1}$	100	0,2	0,01	0,05
P-0,37	0,37	$1,369 \cdot 10^{-1}$	100	0,2	0,01	0,05
P-0,36	0,36	$1,296 \cdot 10^{-1}$	100	0,2	0,01	0,05
P-0,35	0,35	$1,225 \cdot 10^{-1}$	100	0,2	0,01	0,05
P-0,34	0,34	$1,156 \cdot 10^{-1}$	100	0,2	0,01	0,05
P-0,33	0,33	$1,089 \cdot 10^{-1}$	100	0,2	0,01	0,05
P-0,32	0,32	$1,024 \cdot 10^{-1}$	100	0,2	0,01	0,05
P-0,31	0,31	$9,61 \cdot 10^{-2}$	100	0,2	0,01	0,05
P-0,30	0,3	$9,0 \cdot 10^{-2}$	100	0,2	0,01	0,05
P-0,25	0,25	$6,25 \cdot 10^{-2}$	100	0,2	0,005	0,05
P-0,20	0,2	$4,0 \cdot 10^{-2}$	100	0,2	0,01	0,05
P-0,15	0,15	$2,25 \cdot 10^{-2}$	100	0,2	0,005	0,05
P-e-1	0,1	$1 \cdot 10^{-2}$	100	0,2	0,01	0,05
P-e-2	0,01	$1 \cdot 10^{-4}$	100	0,2	0,01	0,05
P-e-3	$1 \cdot 10^{-3}$	$1 \cdot 10^{-6}$	100	0,2	0,01	0,05
P-e-4	$1 \cdot 10^{-4}$	$1 \cdot 10^{-8}$	100	0,2	0,01	0,05
P-e-5	$1 \cdot 10^{-5}$	$1 \cdot 10^{-10}$	100	0,2	0,02	0,05
P-e-6	$1 \cdot 10^{-6}$	$1 \cdot 10^{-12}$	100	0,2	0,02	0,05
P-e-7	$1 \cdot 10^{-7}$	$1 \cdot 10^{-14}$	100	0,2	0,02	0,05
P-e-8	$1 \cdot 10^{-8}$	$1 \cdot 10^{-16}$	100	0,2	0,02	0,05
P-Stability	1,0	1,0	50	0,1	0,01	0,01
P-LongRun	0,1	0,01	200	0,2	0,005	0,05
P-HighRes-0,34	0,1	$1,156 \cdot 10^{-1}$	100	0,2	0,001	0,01
P-HighRes-0,32	0,32	$1,024 \cdot 10^{-1}$	100	0,2	0,001	0,01
P-HighRes-0,31	0,31	$9,61 \cdot 10^{-2}$	100	0,2	0,001	0,01
P-HighRes-0,3	0,3	$9,0 \cdot 10^{-2}$	100	0,2	0,001	0,01
P-HighRes-0,25	0,25	$6,25 \cdot 10^{-2}$	100	0,2	0,001	0,01
P-HighRes-0,1	0,1	$1 \cdot 10^{-2}$	100	0,2	0,001	0,01
P-HighRes-0,01	0,01	$1 \cdot 10^{-4}$	100	0,2	0,001	0,01

Hernquist

Name of the Simulation	χ	η_{vir}	run-time	Δ snap	Δt	ϵ
H-0,95	0,95	$9,025 \cdot 10^{-1}$	100	0,2	0,005	0,05
H-0,90	0,9	$8,1 \cdot 10^{-1}$	100	0,2	0,01	0,05
H-0,85	0,85	$7,225 \cdot 10^{-1}$	100	0,2	0,005	0,05
H-0,80	0,8	$6,4 \cdot 10^{-1}$	100	0,2	0,01	0,05
H-0,75	0,75	$5,625 \cdot 10^{-1}$	100	0,2	0,005	0,05
H-0,70	0,7	$4,9 \cdot 10^{-1}$	100	0,2	0,01	0,05
H-0,65	0,65	$4,225 \cdot 10^{-1}$	100	0,2	0,005	0,05
H-0,60	0,6	$3,6 \cdot 10^{-1}$	100	0,2	0,01	0,05
H-0,55	0,55	$3,025 \cdot 10^{-1}$	200	0,4	0,01	0,05
H-0,50	0,5	$2,5 \cdot 10^{-1}$	100	0,2	0,01	0,05
H-0,45	0,45	$2,025 \cdot 10^{-1}$	100	0,2	0,005	0,05
H-0,40	0,4	$1,6 \cdot 10^{-1}$	100	0,2	0,01	0,05
H-0,35	0,35	$1,225 \cdot 10^{-1}$	100	0,2	0,005	0,05
H-0,30	0,3	$9,0 \cdot 10^{-2}$	100	0,2	0,01	0,05
H-0,29	0,29	$8,41 \cdot 10^{-2}$	100	0,2	0,01	0,05
H-0,28	0,28	$7,84 \cdot 10^{-2}$	100	0,2	0,01	0,05
H-0,27	0,27	$7,29 \cdot 10^{-2}$	100	0,2	0,01	0,05
H-0,26	0,26	$6,76 \cdot 10^{-2}$	100	0,2	0,01	0,05
H-0,25	0,25	$6,25 \cdot 10^{-2}$	100	0,2	0,01	0,05
H-0,24	0,24	$5,76 \cdot 10^{-2}$	100	0,2	0,01	0,05
H-0,23	0,23	$5,29 \cdot 10^{-2}$	100	0,2	0,01	0,05
H-0,22	0,22	$4,84 \cdot 10^{-2}$	100	0,2	0,01	0,05
H-0,21	0,21	$4,41 \cdot 10^{-2}$	100	0,2	0,01	0,05
H-0,20	0,2	$4,0 \cdot 10^{-2}$	100	0,2	0,01	0,05
H-0,15	0,15	$2,25 \cdot 10^{-2}$	100	0,2	0,005	0,05
H-e-1	0,1	$1 \cdot 10^{-2}$	100	0,2	0,01	0,05
H-e-2	0,01	$1 \cdot 10^{-4}$	100	0,2	0,01	0,05
H-e-3	$1 \cdot 10^{-3}$	$1 \cdot 10^{-6}$	100	0,2	0,01	0,05
H-e-4	$1 \cdot 10^{-4}$	$1 \cdot 10^{-8}$	100	0,2	0,01	0,05
H-e-5	$1 \cdot 10^{-5}$	$1 \cdot 10^{-10}$	100	0,2	0,02	0,05
H-e-6	$1 \cdot 10^{-6}$	$1 \cdot 10^{-12}$	100	0,2	0,02	0,05
H-e-7	$1 \cdot 10^{-7}$	$1 \cdot 10^{-14}$	100	0,2	0,02	0,05
H-e-8	$1 \cdot 10^{-8}$	$1 \cdot 10^{-16}$	100	0,2	0,02	0,05
H-St_eps-2	1,0	1,0	50	0,1	0,01	0,01
H-St_eps-3	1,0	1,0	50	0,1	0,01	0,005
H-LongRun	0,1	0,01	200	0,2	0,005	0,05
H-HighRes-0,4	0,4	$1,6 \cdot 10^{-1}$	100	0,2	0,001	0,01
H-HighRes-0,3	0,3	$9,0 \cdot 10^{-2}$	100	0,2	0,001	0,01
H-HighRes-0,25	0,25	$6,25 \cdot 10^{-2}$	100	0,2	0,001	0,01
H-HighRes-0,1	0,1	$1 \cdot 10^{-2}$	100	0,2	0,001	0,01
H-HighRes-0,01	0,01	$1 \cdot 10^{-4}$	100	0,2	0,001	0,01

III.2.2. Disturbed ROI

Rotation

Plummer Setup:

Name of the Simulation	χ	η_{vir}	Ω	run-time	Δ snap	Δt	ϵ
P_O-1e-3_v-001	0,01	$1 \cdot 10^{-4}$	$1 \cdot 10^{-3}$	100	0,2	0,01	0,05
P_O-1e-3_v-01	0,1	$1 \cdot 10^{-2}$	$1 \cdot 10^{-3}$	100	0,2	0,01	0,05
P_O-1e-3_v-02	0,2	$4 \cdot 10^{-2}$	$1 \cdot 10^{-3}$	100	0,2	0,01	0,05
P_O-1e-3_v-03	0,3	$9 \cdot 10^{-2}$	$1 \cdot 10^{-3}$	100	0,2	0,01	0,05
P_O-1e-3_v-035	0,35	$1,225 \cdot 10^{-1}$	$1 \cdot 10^{-3}$	100	0,2	0,01	0,05
P_O-1e-3_v-04	0,4	$1,6 \cdot 10^{-1}$	$1 \cdot 10^{-3}$	100	0,2	0,01	0,05
P_O-1e-3_v-05	0,5	$2,5 \cdot 10^{-1}$	$1 \cdot 10^{-3}$	100	0,2	0,01	0,05
P_O-5e-4_v-001	0,01	$1 \cdot 10^{-4}$	$5 \cdot 10^{-4}$	100	0,2	0,01	0,05
P_O-5e-4_v-01	0,1	$1 \cdot 10^{-2}$	$5 \cdot 10^{-4}$	100	0,2	0,01	0,05
P_O-5e-4_v-02	0,2	$4 \cdot 10^{-2}$	$5 \cdot 10^{-4}$	100	0,2	0,01	0,05
P_O-5e-4_v-03	0,3	$9 \cdot 10^{-2}$	$5 \cdot 10^{-4}$	100	0,2	0,01	0,05
P_O-5e-4_v-035	0,35	$1,225 \cdot 10^{-1}$	$5 \cdot 10^{-4}$	100	0,2	0,01	0,05
P_O-5e-4_v-04	0,4	$1,6 \cdot 10^{-1}$	$5 \cdot 10^{-4}$	100	0,2	0,01	0,05
P_O-5e-4_v-05	0,5	$2,5 \cdot 10^{-1}$	$5 \cdot 10^{-4}$	100	0,2	0,01	0,05
P_O-3e-4_v-001	0,01	$1 \cdot 10^{-4}$	$3 \cdot 10^{-4}$	100	0,2	0,01	0,05
P_O-3e-4_v-01	0,1	$1 \cdot 10^{-2}$	$3 \cdot 10^{-4}$	100	0,2	0,01	0,05
P_O-3e-4_v-02	0,2	$4 \cdot 10^{-2}$	$3 \cdot 10^{-4}$	100	0,2	0,01	0,05
P_O-3e-4_v-03	0,3	$9 \cdot 10^{-2}$	$3 \cdot 10^{-4}$	100	0,2	0,01	0,05
P_O-3e-4_v-035	0,35	$1,225 \cdot 10^{-1}$	$3 \cdot 10^{-4}$	100	0,2	0,01	0,05
P_O-3e-4_v-04	0,4	$1,6 \cdot 10^{-1}$	$3 \cdot 10^{-4}$	100	0,2	0,01	0,05
P_O-3e-4_v-05	0,5	$2,5 \cdot 10^{-1}$	$3 \cdot 10^{-4}$	100	0,2	0,01	0,05
P_O-2e-4_v-001	0,01	$1 \cdot 10^{-4}$	$2 \cdot 10^{-4}$	100	0,2	0,01	0,05
P_O-2e-4_v-01	0,1	$1 \cdot 10^{-2}$	$2 \cdot 10^{-4}$	100	0,2	0,01	0,05
P_O-2e-4_v-02	0,2	$4 \cdot 10^{-2}$	$2 \cdot 10^{-4}$	100	0,2	0,01	0,05
P_O-2e-4_v-03	0,3	$9 \cdot 10^{-2}$	$2 \cdot 10^{-4}$	100	0,2	0,01	0,05
P_O-2e-4_v-035	0,35	$1,225 \cdot 10^{-1}$	$2 \cdot 10^{-4}$	100	0,2	0,01	0,05
P_O-2e-4_v-04	0,4	$1,6 \cdot 10^{-1}$	$2 \cdot 10^{-4}$	100	0,2	0,01	0,05
P_O-2e-4_v-05	0,5	$2,5 \cdot 10^{-1}$	$2 \cdot 10^{-4}$	100	0,2	0,01	0,05
P_O-1e-4_v-001	0,01	$1 \cdot 10^{-4}$	$1 \cdot 10^{-4}$	100	0,2	0,01	0,05
P_O-1e-4_v-01	0,1	$1 \cdot 10^{-2}$	$1 \cdot 10^{-4}$	100	0,2	0,01	0,05
P_O-1e-4_v-02	0,2	$4 \cdot 10^{-2}$	$1 \cdot 10^{-4}$	100	0,2	0,01	0,05
P_O-1e-4_v-03	0,3	$9 \cdot 10^{-2}$	$1 \cdot 10^{-4}$	100	0,2	0,01	0,05
P_O-1e-4_v-035	0,35	$1,225 \cdot 10^{-1}$	$1 \cdot 10^{-4}$	100	0,2	0,01	0,05
P_O-1e-4_v-04	0,4	$1,6 \cdot 10^{-1}$	$1 \cdot 10^{-4}$	100	0,2	0,01	0,05
P_O-1e-4_v-05	0,5	$2,5 \cdot 10^{-1}$	$1 \cdot 10^{-4}$	100	0,2	0,01	0,05

Hernquist Setup:

Name of the Simulation	χ	η_{vir}	Ω	run-time	Δ snap	Δt	ϵ
H_O-1e-1_v-001	0,01	$1 \cdot 10^{-4}$	$1 \cdot 10^{-1}$	100	0,2	0,01	0,05
H_O-1e-1_v-01	0,1	$1 \cdot 10^{-2}$	$1 \cdot 10^{-1}$	100	0,2	0,01	0,05
H_O-1e-1_v-02	0,2	$4 \cdot 10^{-2}$	$1 \cdot 10^{-1}$	100	0,2	0,01	0,05
H_O-1e-1_v-03	0,3	$9 \cdot 10^{-2}$	$1 \cdot 10^{-1}$	100	0,2	0,01	0,05
H_O-1e-1_v-04	0,4	$1,6 \cdot 10^{-1}$	$1 \cdot 10^{-1}$	100	0,2	0,01	0,05
H_O-1e-1_v-05	0,5	$2,5 \cdot 10^{-1}$	$1 \cdot 10^{-1}$	100	0,2	0,01	0,05
H_O-1e-2_v-001	0,01	$1 \cdot 10^{-4}$	$1 \cdot 10^{-2}$	100	0,2	0,01	0,05
H_O-1e-2_v-01	0,1	$1 \cdot 10^{-2}$	$1 \cdot 10^{-2}$	100	0,2	0,01	0,05
H_O-1e-2_v-02	0,2	$4 \cdot 10^{-2}$	$1 \cdot 10^{-2}$	100	0,2	0,01	0,05
H_O-1e-2_v-03	0,3	$9 \cdot 10^{-2}$	$1 \cdot 10^{-2}$	100	0,2	0,01	0,05
H_O-1e-2_v-04	0,4	$1,6 \cdot 10^{-1}$	$1 \cdot 10^{-2}$	100	0,2	0,01	0,05
H_O-1e-2_v-05	0,5	$2,5 \cdot 10^{-1}$	$1 \cdot 10^{-2}$	100	0,2	0,01	0,05
H_O-1e-3_v-001	0,01	$1 \cdot 10^{-4}$	$1 \cdot 10^{-3}$	100	0,2	0,01	0,05
H_O-1e-3_v-01	0,1	$1 \cdot 10^{-2}$	$1 \cdot 10^{-3}$	100	0,2	0,01	0,05
H_O-1e-3_v-02	0,2	$4 \cdot 10^{-2}$	$1 \cdot 10^{-3}$	100	0,2	0,01	0,05
H_O-1e-3_v-03	0,3	$9 \cdot 10^{-2}$	$1 \cdot 10^{-3}$	100	0,2	0,01	0,05
H_O-1e-3_v-04	0,4	$1,6 \cdot 10^{-1}$	$1 \cdot 10^{-3}$	100	0,2	0,01	0,05
H_O-1e-3_v-05	0,5	$2,5 \cdot 10^{-1}$	$1 \cdot 10^{-3}$	100	0,2	0,01	0,05
H_O-5e-4_v-001	0,01	$1 \cdot 10^{-4}$	$5 \cdot 10^{-4}$	100	0,2	0,01	0,05
H_O-5e-4_v-01	0,1	$1 \cdot 10^{-2}$	$5 \cdot 10^{-4}$	100	0,2	0,01	0,05
H_O-5e-4_v-02	0,2	$4 \cdot 10^{-2}$	$5 \cdot 10^{-4}$	100	0,2	0,01	0,05
H_O-5e-4_v-03	0,3	$9 \cdot 10^{-2}$	$5 \cdot 10^{-4}$	100	0,2	0,01	0,05
H_O-5e-4_v-04	0,4	$1,6 \cdot 10^{-1}$	$5 \cdot 10^{-4}$	100	0,2	0,01	0,05
H_O-5e-4_v-05	0,5	$2,5 \cdot 10^{-1}$	$5 \cdot 10^{-4}$	100	0,2	0,01	0,05
H_O-3e-4_v-001	0,01	$1 \cdot 10^{-4}$	$3 \cdot 10^{-4}$	100	0,2	0,01	0,05
H_O-3e-4_v-01	0,1	$1 \cdot 10^{-2}$	$3 \cdot 10^{-4}$	100	0,2	0,01	0,05
H_O-3e-4_v-02	0,2	$4 \cdot 10^{-2}$	$3 \cdot 10^{-4}$	100	0,2	0,01	0,05
H_O-3e-4_v-03	0,3	$9 \cdot 10^{-2}$	$3 \cdot 10^{-4}$	100	0,2	0,01	0,05
H_O-3e-4_v-04	0,4	$1,6 \cdot 10^{-1}$	$3 \cdot 10^{-4}$	100	0,2	0,01	0,05
H_O-3e-4_v-05	0,5	$2,5 \cdot 10^{-1}$	$3 \cdot 10^{-4}$	100	0,2	0,01	0,05
H_O-2e-4_v-001	0,01	$1 \cdot 10^{-4}$	$2 \cdot 10^{-4}$	100	0,2	0,01	0,05
H_O-2e-4_v-01	0,1	$1 \cdot 10^{-2}$	$2 \cdot 10^{-4}$	100	0,2	0,01	0,05
H_O-2e-4_v-02	0,2	$4 \cdot 10^{-2}$	$2 \cdot 10^{-4}$	100	0,2	0,01	0,05
H_O-2e-4_v-03	0,3	$9 \cdot 10^{-2}$	$2 \cdot 10^{-4}$	100	0,2	0,01	0,05
H_O-2e-4_v-04	0,4	$1,6 \cdot 10^{-1}$	$2 \cdot 10^{-4}$	100	0,2	0,01	0,05
H_O-2e-4_v-05	0,5	$2,5 \cdot 10^{-1}$	$2 \cdot 10^{-4}$	100	0,2	0,01	0,05
H_O-1e-4_v-001	0,01	$1 \cdot 10^{-4}$	$1 \cdot 10^{-4}$	100	0,2	0,01	0,05
H_O-1e-4_v-01	0,1	$1 \cdot 10^{-2}$	$1 \cdot 10^{-4}$	100	0,2	0,01	0,05
H_O-1e-4_v-02	0,2	$4 \cdot 10^{-2}$	$1 \cdot 10^{-4}$	100	0,2	0,01	0,05
H_O-1e-4_v-03	0,3	$9 \cdot 10^{-2}$	$1 \cdot 10^{-4}$	100	0,2	0,01	0,05
H_O-1e-4_v-04	0,4	$1,6 \cdot 10^{-1}$	$1 \cdot 10^{-4}$	100	0,2	0,01	0,05
H_O-1e-4_v-05	0,5	$2,5 \cdot 10^{-1}$	$1 \cdot 10^{-4}$	100	0,2	0,01	0,05

Central Mass

Plummer Setup:

Name of the Simulation	χ	η_{vir}	M_{BH}	run-time	Δ snap	Δt	ϵ
P_m_e+2_v-001	0,01	$1 \cdot 10^{-4}$	$1 \cdot 10^2$	100	0,2	0,01	0,05
P_m_e+2_v-01	0,1	$1 \cdot 10^{-2}$	$1 \cdot 10^2$	100	0,2	0,01	0,05
P_m_e+2_v-02	0,2	$4,0 \cdot 10^{-2}$	$1 \cdot 10^2$	100	0,2	0,01	0,05
P_m_e+2_v-03	0,3	$9,0 \cdot 10^{-2}$	$1 \cdot 10^2$	100	0,2	0,01	0,05
P_m_e+2_v-04	0,4	$1,6 \cdot 10^{-1}$	$1 \cdot 10^2$	100	0,2	0,01	0,05
P_m_e+2_v-05	0,5	$2,5 \cdot 10^{-1}$	$1 \cdot 10^2$	100	0,2	0,01	0,05
P_m_e+3_v-001	0,01	$1 \cdot 10^{-4}$	$1 \cdot 10^3$	100	0,2	0,01	0,05
P_m_e+3_v-01	0,1	$1 \cdot 10^{-2}$	$1 \cdot 10^3$	100	0,2	0,01	0,05
P_m_e+3_v-02	0,2	$4,0 \cdot 10^{-2}$	$1 \cdot 10^3$	100	0,2	0,01	0,05
P_m_e+3_v-03	0,3	$9,0 \cdot 10^{-2}$	$1 \cdot 10^3$	100	0,2	0,01	0,05
P_m_e+3_v-04	0,4	$1,6 \cdot 10^{-1}$	$1 \cdot 10^3$	100	0,2	0,01	0,05
P_m_e+3_v-05	0,5	$2,5 \cdot 10^{-1}$	$1 \cdot 10^3$	100	0,2	0,01	0,05
P_m_e+4_v-001	0,01	$1 \cdot 10^{-4}$	$1 \cdot 10^4$	100	0,2	0,01	0,05
P_m_e+4_v-01	0,1	$1 \cdot 10^{-2}$	$1 \cdot 10^4$	100	0,2	0,01	0,05
P_m_e+4_v-02	0,2	$4,0 \cdot 10^{-2}$	$1 \cdot 10^4$	100	0,2	0,01	0,05
P_m_e+4_v-03	0,3	$9,0 \cdot 10^{-2}$	$1 \cdot 10^4$	100	0,2	0,01	0,05
P_m_e+4_v-04	0,4	$1,6 \cdot 10^{-1}$	$1 \cdot 10^4$	100	0,2	0,01	0,05
P_m_e+4_v-05	0,5	$2,5 \cdot 10^{-1}$	$1 \cdot 10^4$	100	0,2	0,01	0,05

Herquist Setup:

Name of the Simulation	χ	η_{vir}	M_{BH}	run-time	Δ snap	Δt	ϵ
H_m_e+2_v-001	0,01	$1 \cdot 10^{-4}$	$1 \cdot 10^2$	100	0,2	0,01	0,05
H_m_e+2_v-01	0,1	$1 \cdot 10^{-2}$	$1 \cdot 10^2$	100	0,2	0,01	0,05
H_m_e+2_v-02	0,2	$4,0 \cdot 10^{-2}$	$1 \cdot 10^2$	100	0,2	0,01	0,05
H_m_e+2_v-03	0,3	$9,0 \cdot 10^{-2}$	$1 \cdot 10^2$	100	0,2	0,01	0,05
H_m_e+2_v-04	0,4	$1,6 \cdot 10^{-1}$	$1 \cdot 10^2$	100	0,2	0,01	0,05
H_m_e+2_v-05	0,5	$2,5 \cdot 10^{-1}$	$1 \cdot 10^2$	100	0,2	0,01	0,05
H_m_e+3_v-001	0,01	$1 \cdot 10^{-4}$	$1 \cdot 10^3$	100	0,2	0,01	0,05
H_m_e+3_v-01	0,1	$1 \cdot 10^{-2}$	$1 \cdot 10^3$	100	0,2	0,01	0,05
H_m_e+3_v-02	0,2	$4,0 \cdot 10^{-2}$	$1 \cdot 10^3$	100	0,2	0,01	0,05
H_m_e+3_v-03	0,3	$9,0 \cdot 10^{-2}$	$1 \cdot 10^3$	100	0,2	0,01	0,05
H_m_e+3_v-04	0,4	$1,6 \cdot 10^{-1}$	$1 \cdot 10^3$	100	0,2	0,01	0,05
H_m_e+3_v-05	0,5	$2,5 \cdot 10^{-1}$	$1 \cdot 10^3$	100	0,2	0,01	0,05
H_m_e+4_v-001	0,01	$1 \cdot 10^{-4}$	$1 \cdot 10^4$	100	0,2	0,01	0,05
H_m_e+4_v-01	0,1	$1 \cdot 10^{-2}$	$1 \cdot 10^4$	100	0,2	0,01	0,05
H_m_e+4_v-02	0,2	$4,0 \cdot 10^{-2}$	$1 \cdot 10^4$	100	0,2	0,01	0,05
H_m_e+4_v-03	0,3	$9,0 \cdot 10^{-2}$	$1 \cdot 10^4$	100	0,2	0,01	0,05
H_m_e+4_v-04	0,4	$1,6 \cdot 10^{-1}$	$1 \cdot 10^4$	100	0,2	0,01	0,05
H_m_e+4_v-05	0,5	$2,5 \cdot 10^{-1}$	$1 \cdot 10^4$	100	0,2	0,01	0,05

IV. Acknowledgements

Ich möchte an dieser Stelle noch einigen Menschen danken, ohne die diese Arbeit nicht möglich gewesen wäre und auch sicherlich nicht so viel Spaß gemacht hätte:

Zuerst Prof. Andreas Burkert, der mir mit dieser Arbeit die Möglichkeit und den Freiraum gegeben hat mich mit meinem Interesse an dem Thema vollkommen auszutoben.

Dann danke ich Dr. Rhea-Silvia Remus, die mich sehr kompetent und intensiv betreut hat. Sie hat mir geholfen wieder einen roten Faden zu finden, wenn mir die oben genannte Freiheit zu viel geworden ist.

Als nächstes möchte ich Dr. Tadziu Hoffmann danken, der mir bei sämtlichen Fortran und Gnuplot Problemen mit viel Geduld und Humor zur Seite gestanden hat.

Bei Felix Schulze bedanke ich mich sehr dafür, dass ich seine velocity-maps für meine Arbeit verwenden durfte. Außerdem dafür, dass er mir geholfen hat einen Denkfehler bei der Bestimmung der Elliptizität zu finden und zu beseitigen. Der Kupferstich seines hochehrwürdigen Antlitzes, der diese Arbeit eigentlich ehrenvoll zieren sollte, war zum Druck der Arbeit leider noch nicht fertig. Möge er für die Masterarbeit bereit stehen!

Vielen Dank auch an Dr. Klaus Dolag, der mich an die grundlegende Arbeitsweise mit dem der Arbeit zugrunde liegenden Code herangeführt hat.

Zudem möchte ich mich bei Alexander Arth bedanken, der mein Interesse für numerische und theoretische Astrophysik geweckt hat und mich von Anfang an dabei unterstützt hat in dem Bereich schnelle Fortschritte zu machen.

Zu guter Letzt möchte ich allen Mitarbeitern und Studenten an der USM danken, die mir bei Fragen zur Verfügung gestanden sind und mich immer unterstützt haben.

V. Selbstständigkeitserklärung

Hiermit erkläre ich, die vorliegende Arbeit selbständig verfasst zu haben und keine anderen als die in der Arbeit angegebenen Quellen und Hilfsmittel benutzt zu haben.

München, am 15. September 2017,

Ludwig Böss